THE DESIGN, EXPERIMENTATION, AND CHARACTERIZATION OF A HIGH-PRESSURE ROUND-EDGED ORIFICE PLATE TEST FACILITY

by

Terence Coulter Casey V

A thesis submitted to Johns Hopkins University in conformity with the requirements for the degree of Master of Science in Mechanical Engineering

Baltimore, Maryland
December 2017

Abstract

Orifice plates are commonly found in fluid measurement devices, piping systems, and engines. They are used as flow measurement devices, appear as restrictors in piping, or are used as fuel injectors inside internal combustion engines. While there are equations that predict the discharge coefficient performance for orifice plates, the most accurate estimates are developed empirically from experimental data, or numerical simulations.

The focus of this thesis is on a sponsor provided round-edged orifice plate under a range of high-pressure flow conditions, with the goal of characterizing the relationship between pressure difference across the orifice and the discharge coefficient, as well as the effect phenomena like cavitation may have. To perform such measurements, a test facility was designed and instrumented to measure the flow rate through and pressure difference across the orifice plate geometry. Additionally, high-speed video of the orifice plate was collected to determine the presence of a range of fluid phenomena, including cavitation and hydraulic flip.

The results show that for the range of pressure differentials tested the orifice plate discharge coefficient is roughly independent of both Reynolds number and cavitation number. Additionally, the asymptotic value of the coefficient is above that predicted for sharp-edged orifice plates and below those for venturi tubes. The high-speed video, recording at frame rates up to 720 fps, shows no evidence of cavitation or hydraulic flip for all experimental pressure differential ranges, 50 to 1200 psid, which indicates that the rounded inlet edge of the orifice delays the onset of cavitation inside the throat of the orifice plate and the flow remains single-phase until exiting. This result, along with the independence of Reynolds number, indicates that for the pressure differential range tested the orifice plate discharge coefficient is only a function of the geometry.

Advisor: Professor Joseph Katz

Readers: Professor Joseph Katz and Professor Rajat Mittal

Acknowledgements

First and foremost, I must thank my family for supporting and helping me throughout my academic career. My sister for showing me what was possible academically, which started in high school and continued through college. She inadvertently gave me my first long-term goal the day she graduated high school at the top of her class. And I have to thank her for softening up our parents for me ahead of time.

Next, my Dad for encouraging my interests in mechanical engineering before I even knew it. Whether it was through disassembling fax machines and PlayStations, or teaching me how to visualize by dropping me off at different intersections in my neighborhood with a map and my bike with the goal of returning home. My ability to understand how components fit together started with him. Finally, I'd like to thank my Mom for doing everything else, whether it was motivating me to finish essays for college, teaching me the importance of how to "serve something up" or, setting the example for how to work diligently (which I don't know if I'll ever really master) her approach set the foundation for who I am.

Next I'd like to thank my sponsor for providing me the opportunity to complete my Master's Degree and funding my research. Through their

understanding I was able to complete all of my course requirements while working without losing my mind. Additionally, their support allowed me to perform research in fluid dynamics and develop my abilities to design, build, trouble shoot, and complete an experiment from start to finish.

Finally, I'd like to thank my advisor, Professor Joseph Katz. Without his willingness to work with my sponsor and me, I would not have been able to do this research, or have a lab space to perform experiments. Also, his insights and comments challenged me to always fully think through a problem before jumping into action. Additionally, I'd like to thank Professor Yury Ronzhes for working with me as I designed my test facility and teaching me about the proper way to design an experiment. Finally, I'd like to thank Barbara Adamson and all the other graduate students who helped me as I conducted my research. Without their help, I would not have received key equipment, been able to set up my test facility or the high-speed camera in a timely fashion.

Table of Contents

List of Figures

List of Tables

Nomenclature

Symbols

β	Ratio of diameters
μ	Dynamic viscosity
ν	Average velocity
ρ	Density
σ	Standard deviation
A	Cross-sectional area
Ca	Cavitation number
Cd	Discharge coefficient
Cv	Flow coefficient
D,d	Pipe diameter
f	Friction factor
g	Gravity
h	Height
H_L	Head loss
L	Length
N	Sample size
p	Static pressure
P1	Pressure at regulator outlet
P2	Pressure upstream of cylinder
P3	Pressure upstream of test section
P4	Pressure downstream of test section
PAC	Pressure after cylinder
PC	Pressure in cylinder
PSS	Steady-state pressure
ΔP12	Nitrogen subsystem pressure differential
ΔP23	Water subsystem pressure differential
ΔP34	Test geometry pressure differential
R	Specific gas constant for N_2
r	Inlet radius of test geometry throat
Re	Reynolds number
T	Temperature
$\dot{V}$	Volumetric flow rate
Δx	Uncertainty

Subscripts

actual	Acutal flow rate
ave,avg	Average
Cyl	Cylinder
ΔArea	Expansion in cross-sectional area
H20	Water subsystem
i	inception
ideal	Ideal flow rate
j	Current time step
j+1	Future time step
j-1	Previous time step
l	General location in flow
m	General location in flow
o	Outlet of general orifice throat
TS	Test section/geometry
V	Vapor
VC	Vena contracta
1	Upstream of general orifice
2	Downstream of general orifice

1 Introduction

1.1 Motivation

The research detailed in this thesis will be used to characterize the discharge coefficient of a specific orifice plate geometry provided by my sponsor for a range of pressure differentials (across the orifice). The orifice plate geometry, which will be described in the following section, is characterized as a round-edged orifice and will be referred to as the test geometry moving forward. Research has shown that while predictions on the discharge coefficient can be made based on generalized equations or numerical simulations, an accurate coefficient requires correlations drawn from experimental results. Additionally, research done has focused mostly on sharp-edged orifices, nozzles, and venturi tubes. All the geometries vary enough that an accurate discharge coefficient for the test geometry cannot be inferred from the results obtained for those geometries.

These differences in the existing research have led to the desire to collect further data for understanding flow through the test geometry. Specifically, the objectives of this research are:

1. Determine the discharge coefficient for the test geometry for a range of Reynolds numbers.

2. To possibly detect the onset and presence of different flow phenomena, such as cavitation, and determine their effects on the test geometry discharge coefficient.

To achieve these objectives pressure measurements were taken both upstream and downstream of the test geometry while a high-speed camera recorded video of the throat of the geometry during each run. Additionally, the flow rate through the facility was measured through a combination of pressure measurements and an ultrasonic flow rate sensor upstream of the test geometry. By comparing the actual flow rate at the test geometry to one predicted by Bernoulli’s equation, the discharge coefficient could be determined.

In the following section, the test facility will be outlined in detail, including the custom acrylic test geometry, a data acquisition system (DAS), two different sides of the test facility (designated by the working fluids, one nitrogen and the other water), and changes made to the facility over the course of the research. The third section outlines the experimental methods including those implemented during testing and those used to analyze the result. The fourth section will present the experimental results and a detailed discussion. The fifth section contains recommendations to the test facility if it is used for future research. Finally, section six will contain the final conclusions drawn from the testing and analysis.

1.2 Background and Governing Theory

Before describing the research conducted in this thesis a brief explanation of the underlying fluid mechanics theory must be presented. The governing theory used in this thesis is Bernoulli's Theorem, which is derived from the Navier-Stokes momentum equations and mass conservation laws for flows under certain conditions (Kundu et al. 2012). For the purposes of this research, the particular case of Bernoulli's equations is for steady state, incompressible, viscous internal flows.

$$p_l + \frac{\rho}{2}\nu_l^2 + \rho g h_l = p_m + \frac{\rho}{2}\nu_m^2 + \rho g h_m + H_L \tag{1-1}$$

First, the subscripts represent two different locations within the same flow, p corresponds to the local static pressure, ν represents the local fluid velocity and h represents the local height. Finally, ρ is the density of the fluid, g acceleration due to gravity, and H_L is an energy loss term referred to as head loss, which is due to viscous effects. With the addition of the continuity equation for incompressible flow, shown below in Equation 1-2, the fluid properties at point l can be determined from knowing the local flow properties at point m or vice versa. Specifically, Equation 1-1 shows that for a given flow under these conditions, the local static and dynamic pressures, along with the fluid height can be related to the same parameters at a different location in the flow while including some energy losses (which can be approximated).

$$\nu_l A_l = \dot{V} \tag{1-2}$$

Above is the continuity equation for an incompressible steady state flow, where $\dot{V}$ represents the constant volumetric flow rate, A represents the cross section area.

In this thesis, the head loss term for straight pipe, H_L, shown in 1-1 has units of pressure (psi).

$$H_L = \rho f \frac{L}{D} \frac{\nu^2}{2} \tag{1-3}$$

Where f is the friction factor, a dimensionless coefficient usually dependent on a combination of the flow and the surface properties of the duct or pipe containing the flow. L and D are both characteristic lengths, normally representing pipe length and diameter respectively. For losses in pipe fittings, an equivalent L/D value is used (Pritchard 2011).

1.3 Flow Through an Orifice

In this subsection, Bernoulli's equation will be applied to flows through an orifice. The term orifice will be used generally for physical geometries where there is a contraction in the internal cross-sectional area through which the flow passes. Examples of this include orifice plates, nozzles, and venturi tubes. These types of orifices can be used in flow meters (Pritchard 2011), but their applications range from nozzles in rockets to restrictor orifice plates in pipe networks as well as fuel injectors in internal combustion engines and beyond.

For orifice plates, there is a further subdivision of sharp-edged versus rounded-edged geometries. For sharp-edged orifices the inlet radius of the geometry is significantly smaller than the throat diameter (r<<d). For round-edged geometries the radius and throat diameter are on a closer order of magnitude (r<d). Nozzles can also be subdivided into two categories as well, converging and de Laval (converging/diverging) nozzles, but will not discussed further.

For orifices at steady state, incompressible flow conditions without any losses, Bernoulli's equation becomes:

$$p_l + \frac{\rho}{2}\nu_l^2 = p_m + \frac{\rho}{2}\nu_m^2 \tag{1-4}$$

Where the locations (l and m) are directly on either side of the orifice geometry, l is upstream and m down downstream. For this thesis, the heights at each point were the same, and therefore cancel each other out. Furthermore, the energy losses through an orifice are represented as a discharge coefficient, C_d, (which will be elaborated on later in this section) as opposed to the head loss term, H_L.

Rearranging the above equation, and substituting in the continuity relation, results in volumetric flow rate at location l, which is shown in Equation 1-5.

$$\dot{V} = A_l \sqrt{\frac{2\Delta p_{lm}}{\rho} \frac{1}{1-\beta^4}} \tag{1-5}$$

$$\beta = \frac{d}{D} \tag{1-6}$$

Here, β refers to the ratio of throat diamter (d) to the upstream pipe diameter (D). Equation 1-5 does not account for any energy loss and is therefore refered to as the ideal flow rate of the flow. The way the energy loss manifests is as a decreased flow rate below the ideal, which is dependent on the pressure differential and geometry. Equation 1-7 shows how the discharge coefficient is calculated.

$$C_d = \frac{\dot{V}_{actual}}{\dot{V}_{ideal}} \tag{1-7}$$

The actual flow rate, $\dot{V}$actual, is directly measured from experimental data. As mentioned previously in the motivation subsection, C_d can vary significantly, as it depends on a variety of features of the flow, fluid used, and geometry. In fact, the range for Cd can be from 0.608 (Smith and Walker 1923) to 0.82 (Lichtarowicz et al. 1965) for sharp-edged orifices. For nozzles and venturis Cd can range from 0.6 (Grey and Wilsted 1949) up to 0.99 (Reader-Harris et al. 2001). Reader-Harris (2015) provides a more indepth review of orifices and their discharge coefficients.

1.4 Cavitation in an Orifice

In the previous subsection single-phase flow through an orifice was examined. For the purpose of this thesis, it does not provide a complete background of the predicted phenomena occurring within the test geometry. The background information must be further expanded to include cavitation and its effects on orifice flow.

Cavitation is the formation of vapor bubbles in a localized region of a flowing liquid due to a sufficiently low static pressure (Brennen 2005). The cause for cavitation inside an orifice can be explained by Bernoulli's theorem when applied to a generic orifice geometry. Figure 1-1 and Figure 1-2 are recreated from Ebrahimi et al. (2017).

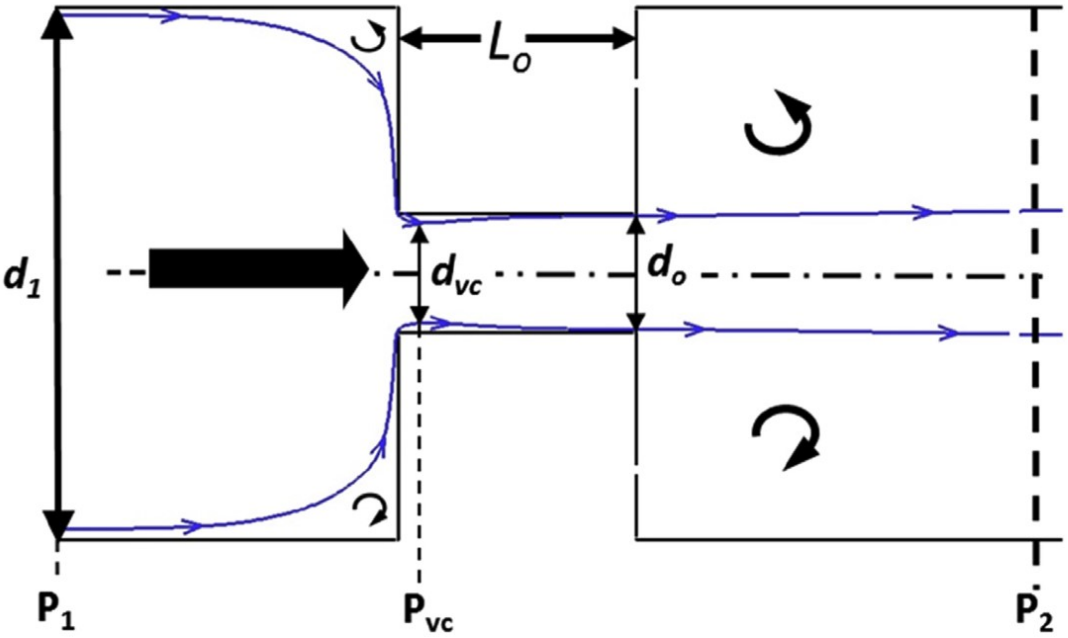

Figure 1-1: Generic orifice with flow contraction and expansion (Ebrahimi et al. 2017).

The above figure represents a generic orifice geometry with streamlines outlining the flow path (from left to right). In the upstream section of the geometry (from d_1 to d_{vc}), the fluid velocity is relatively low and the local static pressure remains high. As the fluid moves downstream into the throat of the orifice (d_{vc} to d_o) the flow accelerates. This acceleration results in the local static pressure dropping, which can be seen in Bernoulli's equations for steady-state flow, and the appearance of what is called a vena contracta. At this location the cross-sectional area and static pressure of the flow is the smallest, and therefore the velocity is the highest.

Generally, if the local mean pressure at the vena contracta, P_{vc}, is above that of the vapor pressure, P_v, no vapor bubbles form and the flow remains single phase. This does not account for turbulence, and flow separation, which could cause pressure fluctuations that result in local intermittent pressures below the vapor pressure, while the mean pressure is above vapor pressure. This typically occurs in shear layers, separated regions, and jets. If P_{vc} drops below P_v then vapor bubbles will form (cavitation). This will also lead to separation of the liquid flow from the throat surface. If this flow separation reaches the end of throat, hydraulic flip will occur. This is where a thin film of air from downstream of the throat recirculates along the surface of the throat.

After the vena contracta, the flow will expand slightly, filling the throat diameter, d_o, causing in a slight increase in the local static pressure, P_o. If P_o is above P_v, then the cavitation bubble will collapse before exiting the throat. Finally, the fluid exits the orifice, leading to an eventual expansion of the flow and increase in static pressure with a decrease in velocity. Figure 1-2, shown below, was also recreated from Ebrahimi et al. (2017), and shows the accompanying pressure curves for single-phase flow through an orifice (a), as well as cavitating flow (b).

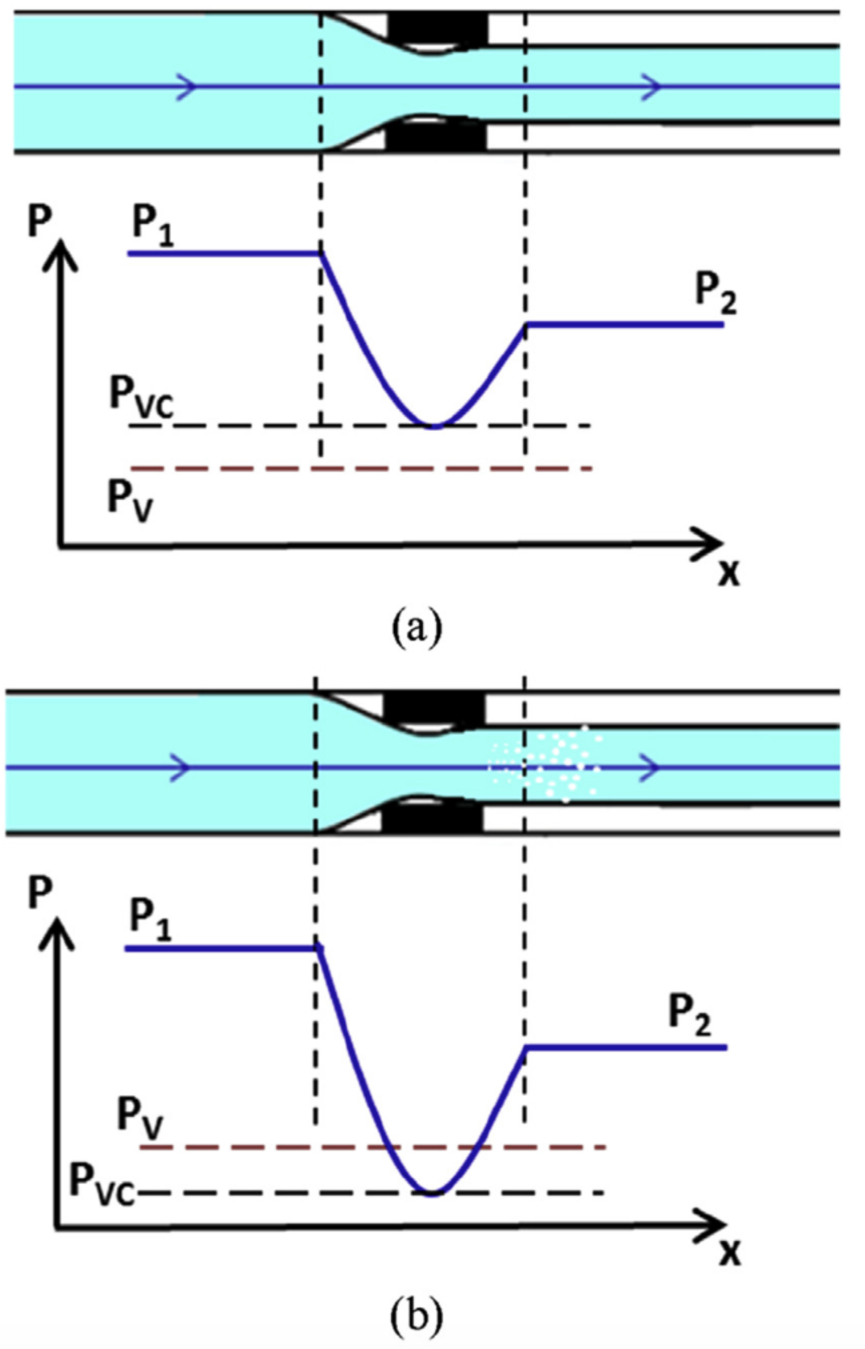

Figure 1-2: Pressure curves of (a) non-cavitating and (b) cavitating flow through an orifice (Ebrahimi et al. 2017).

As mentioned, above for cavitation to occur the local static pressure must be sufficiently close to or below the vapor pressure of the liquid. The standard method to characterize this is with the non-dimensional Cavitation number, Ca, which is defined in the equation below.

$$Ca = \frac{p_l - p_\nu}{\frac{1}{2}\rho\nu_l^2} \tag{1-8}$$

Here p_l and p_v is the local static and vapor pressure respectively. The fluid density is represented by ρ and ν represents the velocity. It is conventional to associate cavitation inception to a specific cavitation number, Ca_i, which may vary from the cavitation number when the local static pressure is equal to the fluid vapor pressure, Ca_v. This is due to many factors that may cause Ca_i to differ from Ca_v (Brennen 2005). These factors are not covered in this text; however, some are discussed in Brennen (2005) and Billet (1985). A summary of inception data is also provided in Brennen (1995).

Once cavitation inception occurs, typically in the inlet of the orifice throat, it can be assumed the initial bubble size is microscopic and not visible to the naked eye (Brennen 2005). For basic bubble growth and collapse theory the Rayleigh-Plesset equation (Plesset 1949) is used. While a full description of the equation and phenomena is not warranted as it is outside the scope of this thesis, it should be mentioned for completeness.

As the bubble grows inside the throat of the orifice, it becomes visible and reaches a critical radius, after which, it becomes unstable and collapses. This radius, typically called the Blake critical radius was first identified by Blake (1949) as well as Neppiras and Noltingk (1951); however, for the vapor bubble to grow it must spend a sufficient amount of time within the low-pressure region of the throat. If the flow velocity is too high, the bubble will pass through the throat before it can grow to an unstable size and remain invisible to the naked eye (Brennen 2005).

Finally, if the bubble is able to reach an unstable radius and collapse, the effects can cause major damage to solid surfaces in the vicinity (ATSM 1967). This damage is due to the micro-jets of water created as the bubble collapses near the wall. The violent collapse leads to extremely high pressures, which can reach 848 bar (Fujikawa and Akamatsu 1980) for fractions of a second. These conditions lead to erosion and fatigue of the orifice material, which is why determining the presence of cavitation has been extensively researched and its detection is within the scope of this thesis.

1.5 Literature Review

To provide an organized and concise review of the research conducted thus far, this section will be divided into two subsections; the first will focus on single-phase flow research, and the second will be on multiphase flows. These subsections will primarily address orifice plate geometries but will discuss others, such as nozzles, for a more in-depth review.

The characterization of the discharge coefficient for an orifice has been a subject of research dating back to at least the 1920s, with it growing in interest into the 1940s, and through the 1960s as the use of rockets in aircraft became more prevalent. Initially the research focused on characterizing the discharge coefficient for a very basic array of parameters.

Smith and Walker (1923) is one of the first papers, which aimed to experimentally produce a relationship between the discharge coefficient, the head supply, orifice diameter, vena contracta diameter, and upstream pipe diameter. Their research resulted in discharge coefficients, which ranged from 0.61 to 0.68 for different orifice diameters (0.75” to 2.5”) and head supply (0.2’ to 100’). Additionally, it showed an exponential decay relationship between discharge coefficient and head supply.

Next, G. W. Hall (1963) presented an analytical approach to determining the discharge characteristics of long-tube orifices ($1 < L/D < 10$) with the application of boundary-layer theory. Hall also looked at the effect of inlet geometries, specifically chamfered and rounded edges. The results were compared to previous experimental work, and could be applied to a range of Reynolds numbers (Re), the equation for which is shown below, between 10^3 and 10^5. The results allowed for orifice designs to be "rated" on a theoretical basis, without the use of experimentation for the proposed geometry. Hall also discussed the effect a rounded inlet has on the flow; specifically, delaying the onset of a turbulent boundary layer and flow separation from the orifice wall.

$$Re = \frac{\rho \nu d}{\mu} \tag{1-9}$$

Equation 1-9 defines the generalized Reynolds number, Re, where d is a characteristic length, and for this thesis it is the pipe diameter. The fluid dynamic viscosity is represented by μ.

Lichtarowicz et al. (1965) summarized previous research, as well as added to Hall's work by experimentally measuring the discharge coefficient for similar long orifice geometries in the same range of Reynolds numbers (up to 10^5). Results from Lichtarowicz et al. show that the discharge coefficient of an orifice resembles a logarithmically increasing relationship, with respect to Reynolds number for all L/D ratios. Additionally, the largest asymptotic discharge value was typically 0.8, and became independent of Reynolds number at values of 10^4. Kiljański (1993) also showed similar dependence on Reynolds number for a range of L/D values and different orifice diameters for Reynolds numbers below 10^3. Results from

Lichtarowicz et al. for a L/D = 2 are shown below. This is the same geometric ratio for the test geometry presented in this thesis.

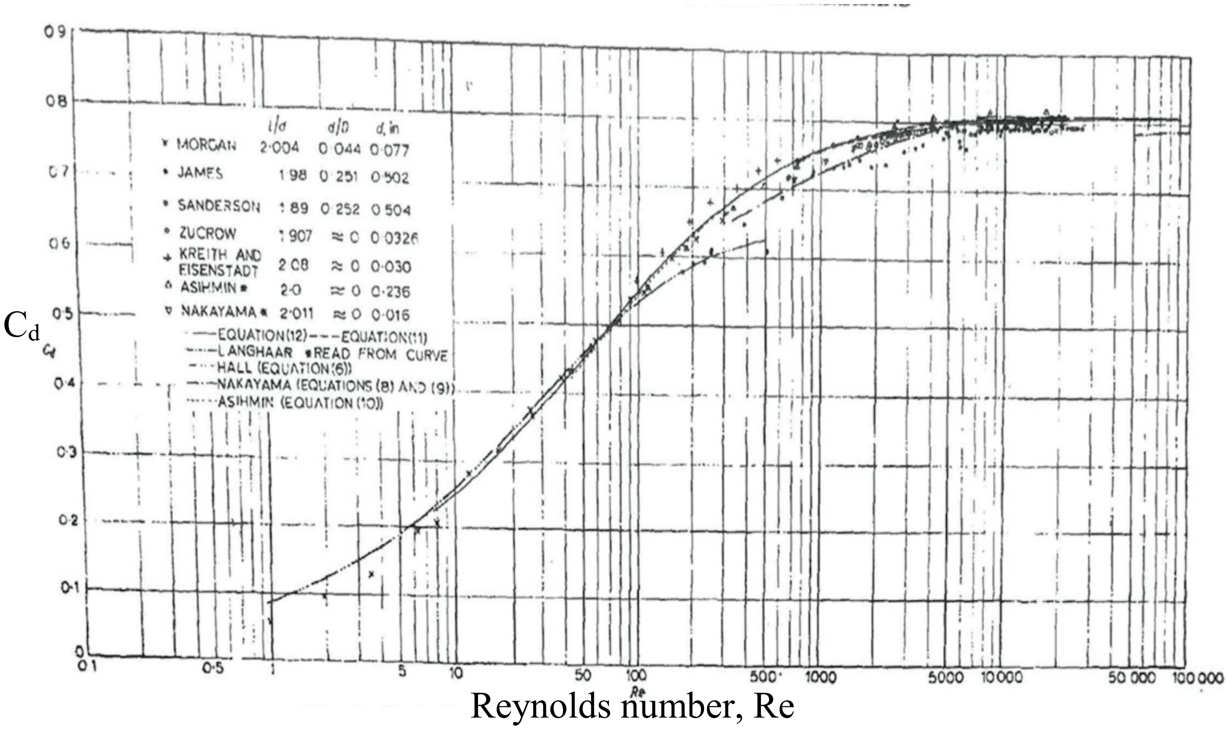

Figure 1-3: Variation of discharge coefficient with Reynolds number, L/D=2 (Lichtarowicz et al. 1965).

Wu Jianhua (2010) further supports and extends the range of these results to Re > 10^5 by showing the discharge coefficient is dependent on the inlet and contraction geometry and becomes roughly independent of Reynolds number at Re > 10^5. Wu Jianhua showed this result by using a combination of numerical simulations and model experiments.

After Lichtarowicz et al. and Hall's work, which focused primarily on the effects L/D had on discharge coefficient, Hobbs and Humphreys (1990) examined the effect of rounding the inlet edge of the orifice. The results showed discharge coefficient increased with increased rounding of the upstream edge.

Other orifice research shows a similar historical trend, starting with experiments, and then analytical solutions are developed and compared to the existing data. Grey and Wilsted (1949) performed experiments to determine the effect basic geometric differences had on discharge coefficient for subcritical flows in a nozzle. Their research included varying the inlet converging angle and the inlet-outlet diameter ratio (equivalent to the throat to inlet diameter ratio for orifice plates) over a range of Reynolds numbers from 10^5 to 10^6.

The results showed a similar logarithmically increasing asymptotic behavior of discharge coefficient for all variations of both converging angle and inlet outlet diameter pressure ratio. The discharge coefficient range was much larger compared to orifice plates, ranging from 0.6 to almost reaching unity; however, no one configuration spanned the entire range, and a summary plot recreated from the research is shown below.

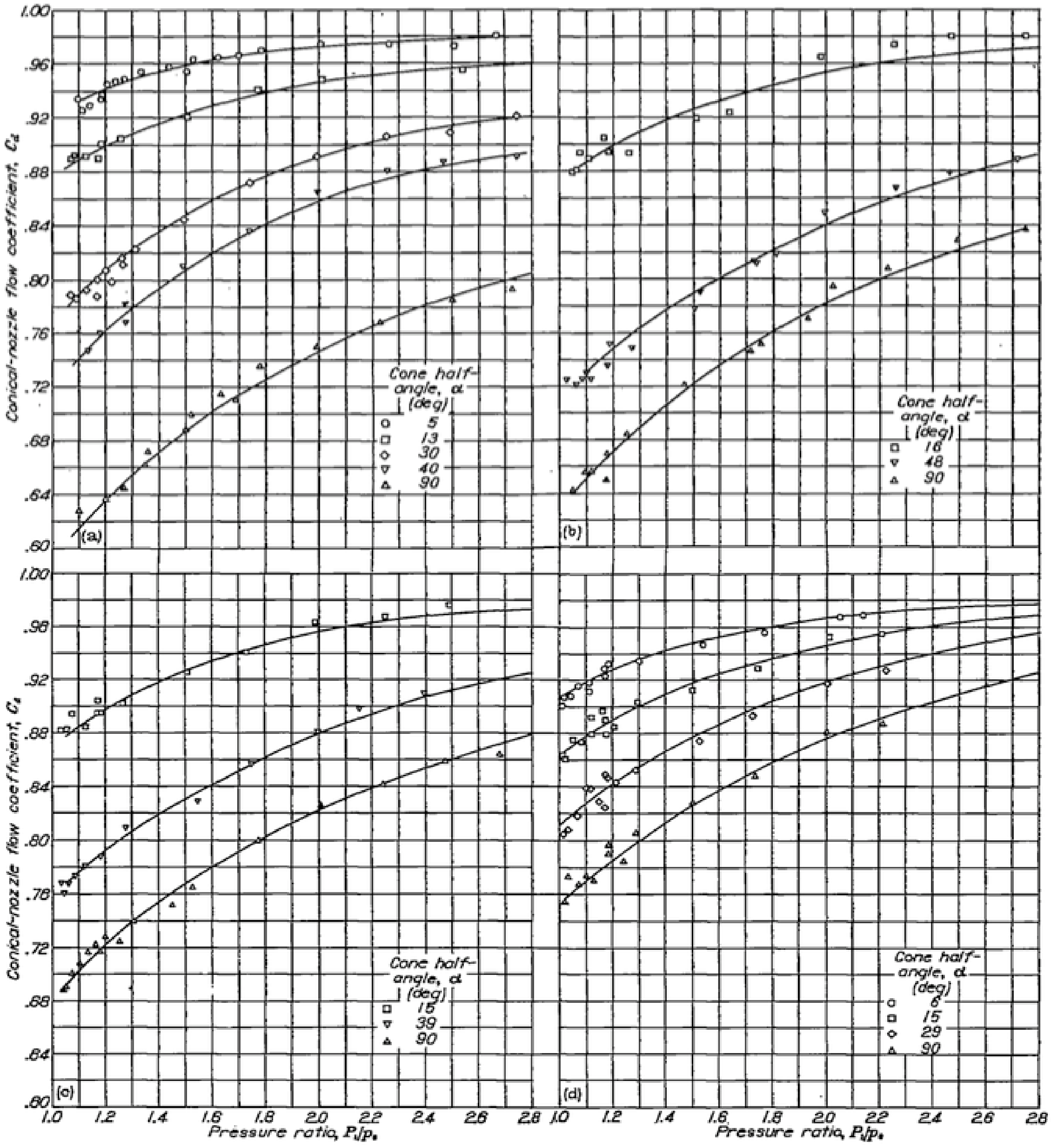

(a) Outlet-inlet diameter ratio, 0.50.
(b) Outlet-inlet diameter ratio, 0.67.
(c) Outlet-inlet diameter ratio, 0.80.
(d) Outlet-inlet diameter ratio, 0.91.

Figure 1-4: Variation of discharge coefficient with pressure ratio for varying inlet nozzle geometries (Grey and Wilsted 1949).

Hebbar et al. (1969) then used results from Grey and Wilsted (1949) to determine an analytical expression for a general nozzle discharge coefficient. They were able to expand on Grey and Wilsted (1949) by confirming that the discharge coefficient increases with increasing pressure differential and decreased with increasing inlet convergence angle.

After initial experimentation and subsequent development of analytical expressions, further research was completed to see how smaller changes to nozzle geometry affected discharge coefficient. One such paper was Kent and Brown (1983), which discussed the effect square-edged versus rounded inlet geometries had on nozzle flow for internal combustion engines at Reynolds numbers below the previous work mentioned ($\sim 10^4$). The results confirmed the same findings from orifice plate research, which was that the rounded inlet increased the average discharge coefficient. In this case it increased from ~0.8 to ~0.95. In addition, Kent and Brown (1983) showed that for both sharp-edged and rounded nozzles, the discharge coefficient was independent of the range Reynolds numbers tested.

More recent research still focuses on the discharge coefficient of engine nozzles, but now looks to develop a theoretical model, in conjunction with computer modeling. These models can be applied to a larger range of flow conditions, since the experimental research like Kent and Brown (1983) is only valid for the flow conditions tested. Desentes et al. (2016) presents both a theoretical and experimental study to confirm their results. Much like

Hall (1963), boundary layer theory was used to develop the theoretical model, and their results showed good comparison with previous research. These results showed the same asymptotic behavior for the discharge coefficient for Reynolds numbers on the order of 10^4.

In addition to the research being conducted on single-phase flows through orifices, multiphase flows through orifices were also being studied. These experiments typically investigated both single and multiphase flow regimes as it allowed researchers to compare the effects of cavitation on discharge coefficient to non-cavitating flows as well. One such paper was from Spikes and Pennington (1959), which looked at the effects cavitating flows had on submerged orifices.

Similar to the single-phase flow papers, their research also included the effects of variations in L/D and inlet geometry. Their results showed good agreement with previous research for discharge coefficient values and asymptotic behavior for similar Reynolds numbers. They also discussed how to mitigate the effects of cavitation on discharge coefficient. Specifically, they showed that by decreasing L/D, the location where cavitation occurs can be moved downstream of the orifice, and then it has no effect on the flow. Spikes and Pennington (1959) also showed the association between the presence of cavitation and sharp-edged orifices.

They recommended rounding the inlet geometry with a chamfer to delay the onset of cavitation for a given Reynolds number.

This insight leads into another area of research, which is determining the onset (or inception) of cavitation based on flow and geometric parameters. Ramamurthi and Nandakumar (1999) discussed the geometric effects of L/D and orifice diameter on cavitation. Their results showed that for increasing L/D the cavitation number at inception was delayed. This provides an additional approach to mitigate the effects of cavitation on the discharge coefficient. Their research also included a numerical model of cavitation bubble collapse based on the Rayleigh-Plesset equation. They concluded that the non-dimensional length over which a bubble collapseed is approximately 1.9 for inviscid flows in sharp-edged orifices. They speculated, based on data, that the collapse occurred over a length closer to L/D = 5 for viscous flows. This provided an upper limit for L/D before cavitation may occur within the orifice. Their comparison of discharge coefficients for non-cavitating and cavitating flows also shows that there was a drop in the coefficient to ~0.6 once cavitation occurred for some L/D values, and again the coefficient became independent of Reynolds number. This was confirmed by Chemloul (2011). Chemloul looked at the effects cavitation and hydraulic flip had on the sharp and round-edged orifices at a variety of L/D values and pressure differentials. A summary plot of the discharge coefficient results from Chemloul (2011) is shown below.

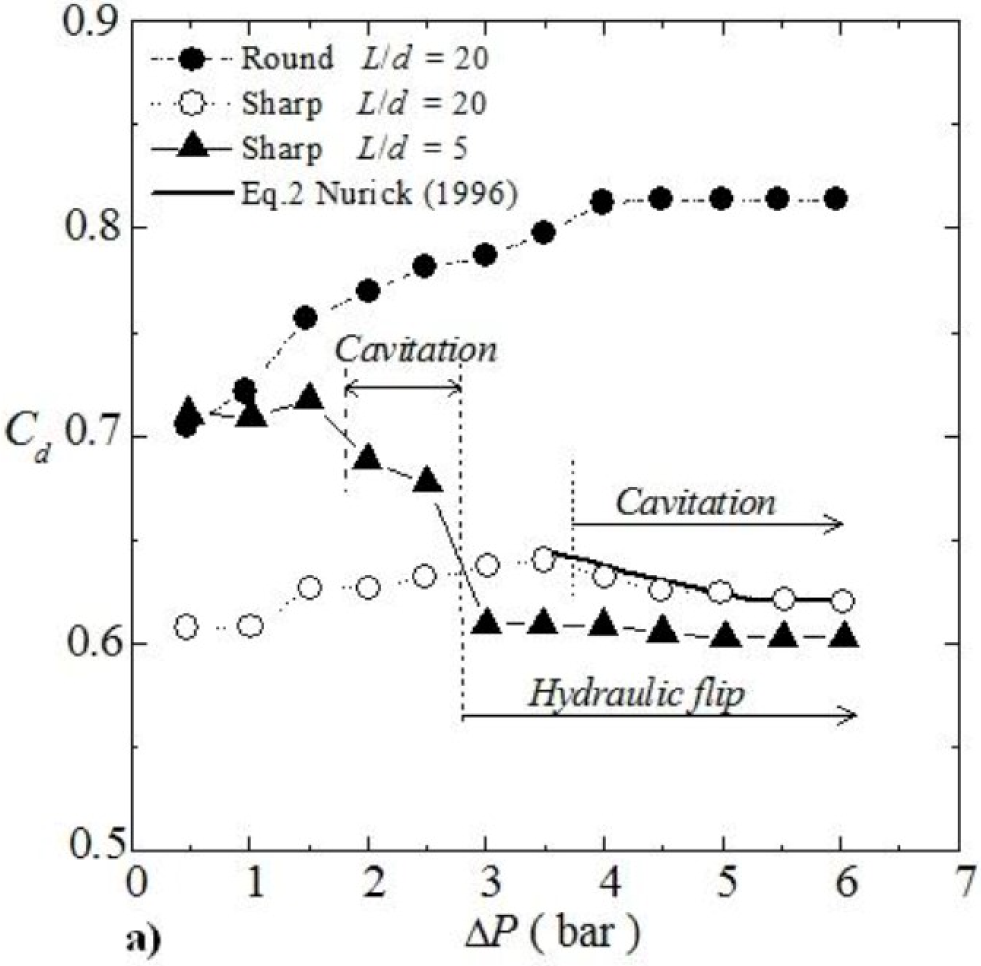

Figure 1-5: Comparison of discharge coefficient for non-cavitating, cavitating and hydraulic flip flows (Chemloul 2011).

Finally, due to advancements in computing, simulations are now used in addition to experimental and theoretical work for cavitating flows. Two such papers are Ebrahimi et al. (2017) and Ashrafizadeh and Ghassemi (2014) both used ANSYS FLUENT computational fluid dynamics (CFD) software, with the first looking at thick orifice plates and the latter studying venturi tubes. Ebrahimi et al. (2017) focused on both choked and non-choked flows and compared cavitating flows to non-cavitating flows to investigate the onset of the phenomena. Their results included discharge coefficients of ~0.8 for non-choked flow and a range of coefficients from ~0.6 to 0.78 for choked flow. The Reynolds numbers for their research ranged between $2x10^5$ to $2x10^6$ and showed that basic theory does not accurately predict discharge coefficients for such high Reynolds number flows due to an oversimplification of the phenomena. Additionally, CFD provided insights into which conditions would cause cavitation and choking to occur. Ebrahimi et al. (2017) also showed that the model was in good agreement with the experimental data, but not necessarily simply theory.

Through this literature review, a brief history of research into both non-cavitating and cavitating flows in orifices was explored. This included experimental, theoretical, and computational investigations into the subject. The overarching conclusions from this review are:

1. Orifice plates typically exhibit a lower discharge coefficient compared to other orifice geometries.
2. Rounding of the inlet geometry allows for an increase in discharge coefficient and delays the onset of cavitation within the orifice.

3. Typically, for increasing Reynolds number, there is a logarithmic increase in discharge coefficient for both single and multiphase flows up to a maximum coefficient value.
4. The asymptotic value of a discharge coefficient is dependent only on the orifice geometry.
5. To mitigate the effect of cavitation on discharge coefficient, L/D must either be small so that the phenomena occurs downstream of the orifice or large enough as to allow the bubble to collapse and reattach to the orifice wall with potentially negative effects the orifice material.
6. Theoretical and computation derivations of discharge coefficients relay on experimental data for validation, and can differ from real values if their derivations are over-simplified.

2 Experimental Design and Facility

For this research, experiments were conducted using a test facility that was designed and built in the Laboratory for Experimental Fluid Dynamics at Johns Hopkins University Homewood Campus. The overall design of the test facility consisted of two separate piping subsystems, which were differentiated by the working fluid in each part. The first subsystem's working fluid was water, and the test geometry was located here. The second subsystem's working fluid was nitrogen gas (N_2) and acted as the high-pressure source, which drove the liquid through the orifice. The interface between the two subsystems was a high-pressure cylinder that contained a piston. During each test, high-pressure nitrogen pressurized one side of the piston, moving it down the cylinder's length, pushing water through the test geometry. Before the facilities were designed and built, several technical requirements were identified that needed to be met.

2.1 Technical Requirements

Listed below are the identified design requirements for the test facility:

1. The test facility shall allow for a pressure difference of up to 2500 psid across the test geometry for each experiment.

2. The test facility shall accommodate a range of different data collection instruments to allow for multiple methods to investigate the phenomena inside the test geometry during a test.
3. The test facility shall allow for pressure transducers to be located directly upstream and downstream of the test geometry.
4. The test geometry shall be transparent to allow for high-speed video recording of the flow during each run.
5. The test facility shall store enough water at test pressure (up to 2500 psid) to allow for steady state conditions[*] during the majority of a run (approximately three seconds).
6. The test geometry will be consistent with the geometry provided by the sponsor.
7. The test facility will use water as the working fluid.
8. All piping and hoses must be made of materials that will not corrode in the presence of water, i.e. stainless steel.

---

[*] Steady State Conditions shall be defined later in Section 3: Experimental Methods

2.2 Test Section

The test section was comprised of four separate components. These parts were the orifice test block, which housed the test geometry, the inlet and outlet flanges, which mounted directly upstream and downstream to the test block respectively, and the flange pipe adapter, which allowed for the test section to be connected via National Pipe Taper (NPT) threads to the rest of the test facility. The technical drawings for each test section component, and one of the entire assembly, can be found in Appendix A.

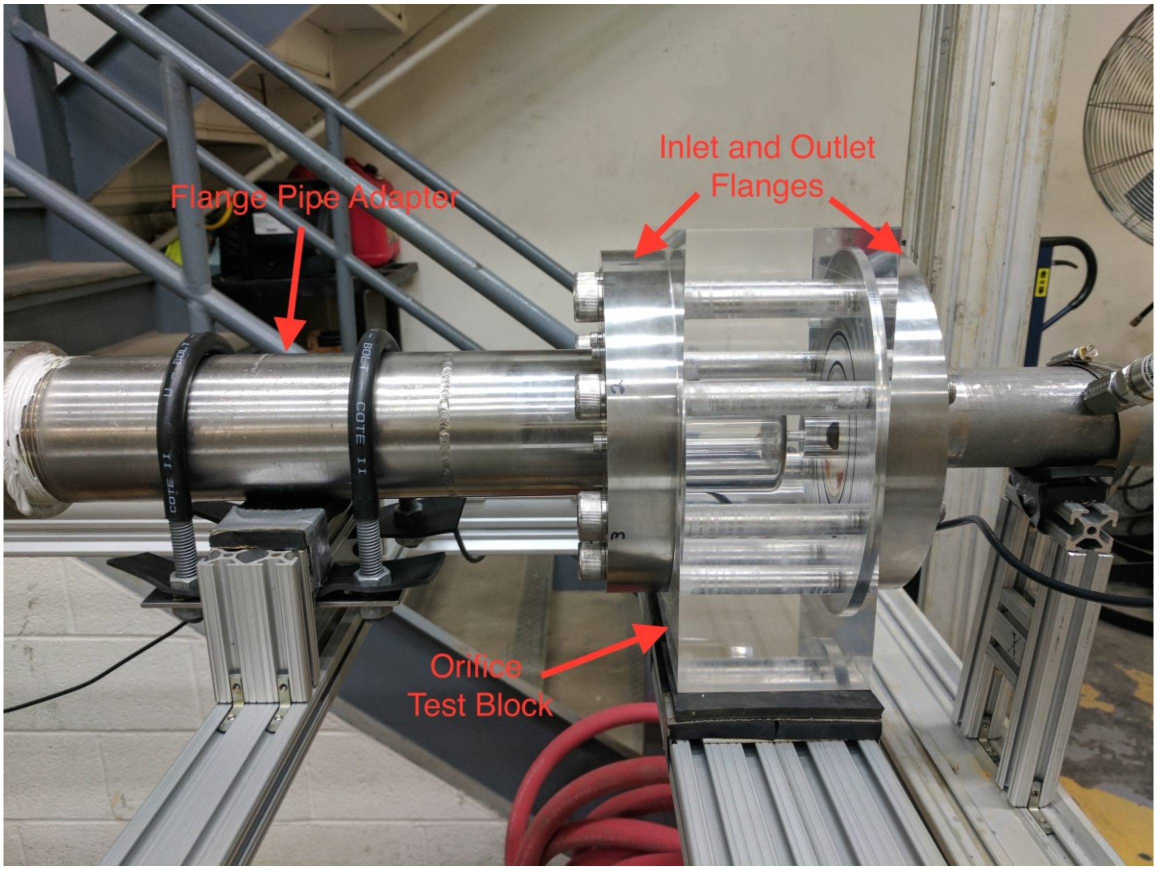

Figure 2-1: Image of test section installed in test facility.

2.2.1 Orifice Plate Test Block

The orifice plate test block was machined from a solid 12” x 12” x 4” cast acrylic block. Below, Figure 2-2 shows the required dimensions for machining the test block.

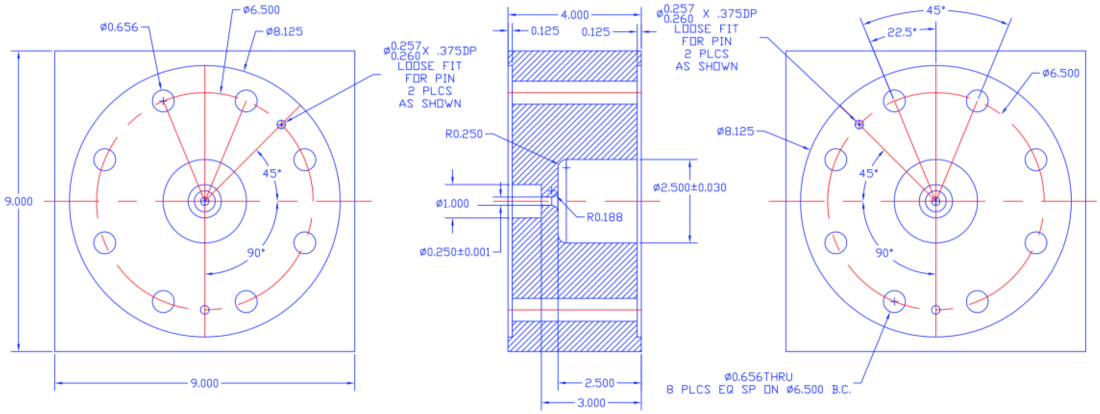

Figure 2-2: Diagram of orifice plate test block with front, back and cross-sectional views and all relevant dimensions.

Upstream Diameter (in)	2.50
Throat Diameter (in)	0.25
Inlet Radius (in)	0.188
Plate Thickness (in)	0.50
Downstream Diameter (in)	1.00

Table 2-1: Key orifice geometry dimensions.

While the thickness, throat diameter, nozzle radius and upstream diameter where provided by the sponsor; the downstream diameter of the orifice plate, and radial thickness of the test block were calculated based on safety requirements. The downstream diameter of the orifice plate was determined by performing a basic cantilever beam analysis of the orifice plate geometry (Beer et al. 2011). For this analysis the plate was “cut” into eight sections in the radial direction to make individual cantilever beams. The width was assumed to be the average of the inner edge (1/8 circumference of the throat) and outer edged (1/8 the circumference of the upstream diameter). The thickness was ½” and the cross sectional shape was a rectangle. A uniform load of 2500 psid (the maximum pressure differential across the orifice plate) was used as the applied force and a safety factor of 1.67 was also implemented. Using these parameters, the maximum length of the beam was calculated such that the maximum stress did not exceed the shear/yield strength of the acrylic.

As the plate was not a collection of independent cantilever beams, it was assumed this approach was adequate and the design would provide sufficient strength to prevent the acrylic from cracking and blowing out. The small safety factor was selected so if failure did occur in the test block, it would be in the axial direction. This would allow the acrylic to safely move downstream in pipe, which is visible in Figure 2-1. If the acrylic failed radially, there was no additional shielding to absorb the acrylic pieces.

The dimensions of the inlet and outlet flanges also drove the height and width of the acrylic block, but the radial stresses were calculated to confirm the test block was sufficiently thick (Beer et al. 2011).

The thickness was defined by the difference in the upstream diameter radius (2.5”) to the center of the bolt holes. The resulting safety factor was ~8, which was more than enough to successfully prevent the test block from failing radially. In addition to these design considerations, the bolt-hole pattern was selected such that the test geometry could be viewed 90° angles apart without obstruction. Two 8.125” wide, 0.125” wide circular recesses were milled on the upstream and downstream faces of the test block as well. These recesses, along with holes drilled in the face for press-fitted pins, ensured the test section could be reassembled in the same orientation every time.

After machining, both the inside and outside of the block was polished to ensure the test block was optically clear for high-speed video. Figure 2-3 shows the test block before and after polishing. Due to geometric constraints, the parallel portion of the test geometry throat could not be polished to be completely optically smooth; however, it still met the surface roughness requirements provided by the sponsor.

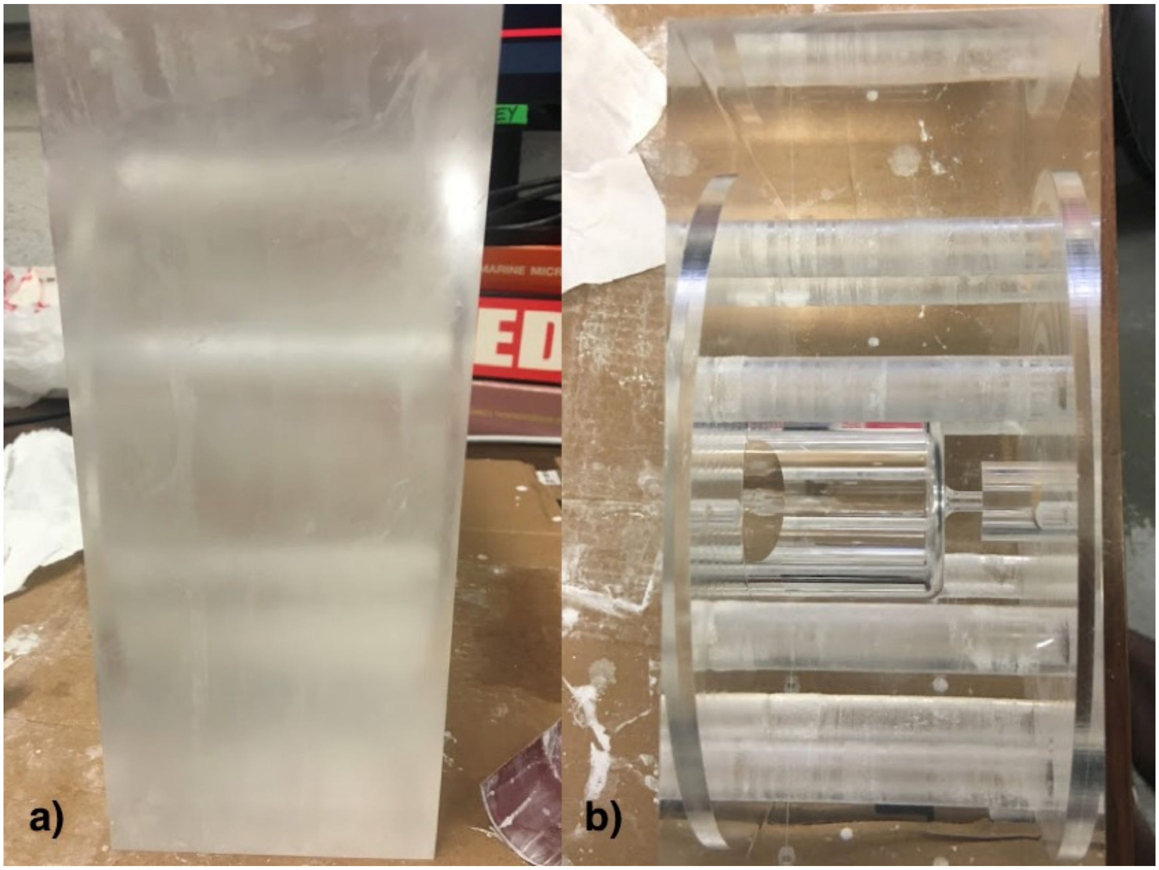

Figure 2-3: Acrylic test block (a) before and (b) after polishing.

2.2.2 Inlet and Outlet Flanges

Both the inlet and outlet flanges for the test facilities were based on the same flange design. There were some differences in each flange to account for their specific pipe fittings. As stated in the design requirements section, all piping in the water subsystem of the test facility must be made from non-corroding materials, this resulted in the custom designed flanges.

They were based on the design of a high-pressure steel pipe flange for size 2 NPT pipe, which met the following specifications: ANSI/ASME B16.5 Class 1500 Threaded Flanges. This class of flanges is rated for a working pressure of 3000 psig or above, which is sufficiently above the working pressure of the test geometry (~2500 psig). The same flange outer diameter, thickness, bolt-hole pattern and location were used for the custom flanges as those that met the ASME specifications.

The only major variation was instead of a gasket being used to seal the flanges against the test block, a series O-rings were used. This was done so the flanges and test block could mate in the same orientation during reassembly of the test section with metal pins. The groove design for the O-rings is outlined in the Parker O-ring Handbook (2011). For this type of application, the handbook specified that two different sized O-rings to be used. The two sizes were 2-347 and 2-337.

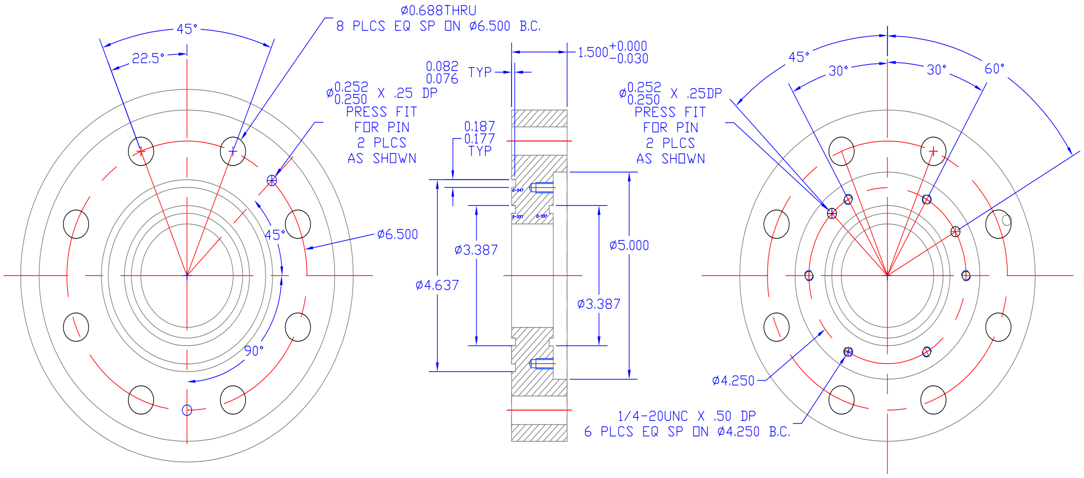

Figure 2-4: Dimensions of inlet flange.

The pipe connection for the inlet flange was not threaded as the ASME flange; this was done to prevent any adverse effects to the flow directly before the test block. Instead, the inner diameter of the flange matched the upstream diameter of the test block (2.5”). It was also designed to smoothly mate with the inlet flange pipe adapter. Again, to ensure the two components could be reassembled in the same orientation a pin was used with an O-ring to seal the connection. This O-ring design was also based on the Parker O-ring Handbook (2011).

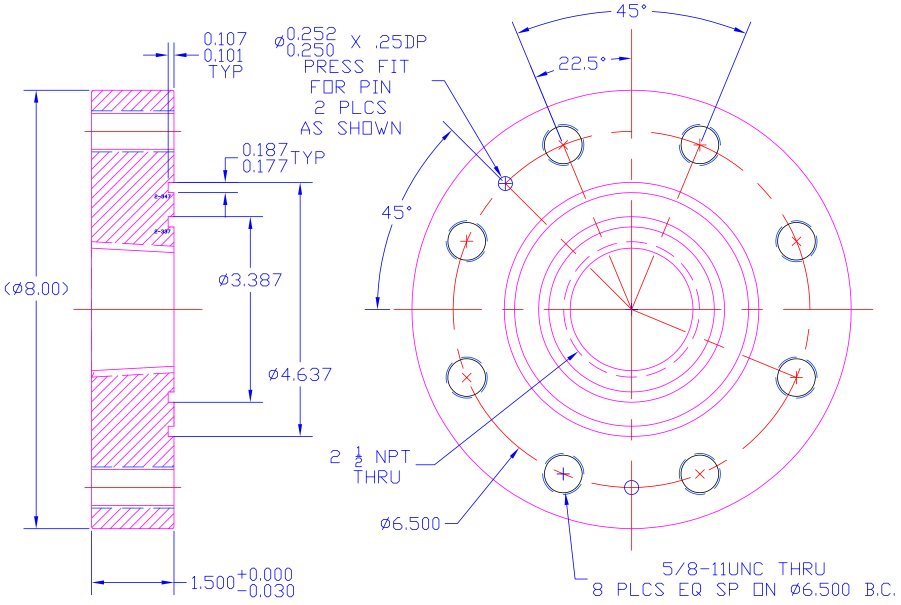

Figure 2-5: Dimensions of outlet flange.

For the downstream flange, the inner pipe thread was 2 ½ NPT oppose to size 2 NPT. During testing, the pressure downstream of the flange actually never exceeded 100 psia. So this increase in diameter did not affect the overall safety of the test facility.

2.2.3 Flange Pipe Adapter

The flange pipe adapter allowed the test section to be connected to standard pipe thread (NPT) while maintaining a smooth interior pipe surface. This was required so there was no chance of variation in the flow directly before the test geometry. It also allowed for the test section to connect to a larger pipe diameter upstream. The reason for using the larger pipe diameter will be provided in the following subsection (2.2.4 Water Subsystem). Additionally, the flange pipe adapter had two 0.125” NPT ports 90° apart along the circumference. A pressure transducer was placed in one port and was used to record the static pressure directly before the test geometry. The other port, which was oriented vertically, was used to bleed off any air trapped in the water subsystem before each run.

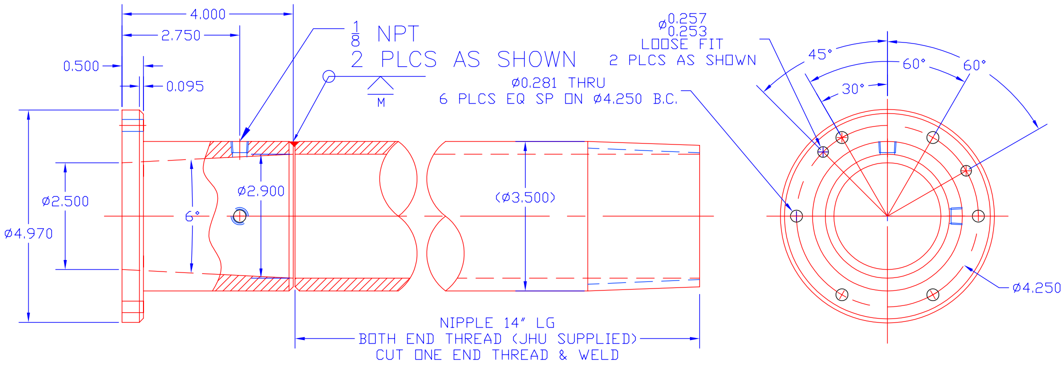

Figure 2-6: Dimensions of flange pipe adapter.

2.3 Water Subsystem

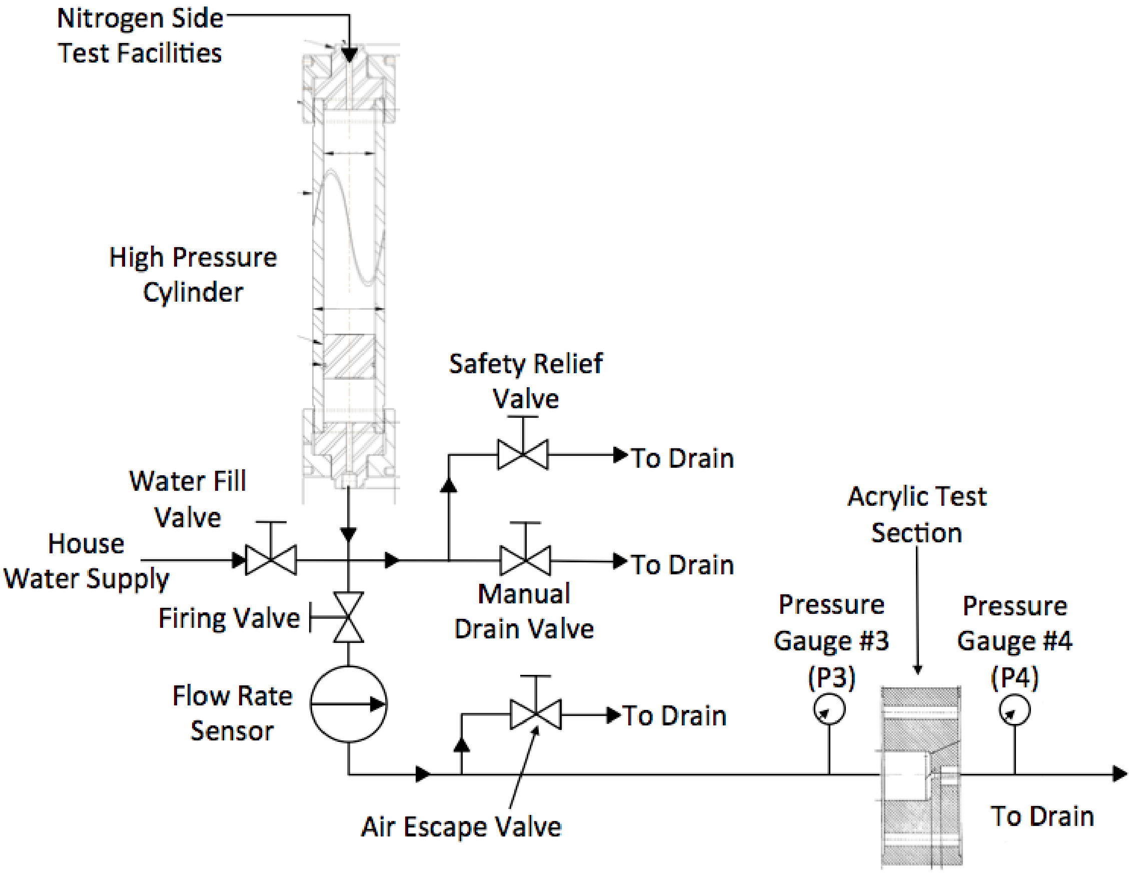

Figure 2-7: Schematic of test facility water subsystem.

The water subsystem of the test facility, shown above, was an atmospheric system, which allowed for high-pressure water to flow through the round-edged orifice (the test geometry), then to the lab facility's drain. It was supplied with house water that was filtered through a two-stage system using 20 micron and 5 micron sized filters. All pipes in the water subsystem were stainless steel and rated for 3000 psi or above to prevent the formation of any rust inside the pipe. Each threaded connection was sealed with Loctite 5113, a high-pressure thread sealant.

The water subsystem worked by filling the high-pressure piston, which will be discussed in Section 2.5, with water, then isolating the upstream side of the water subsystem by closing the water fill, air escape, and firing valves. Once the system was pressurized via the nitrogen subsystem, the firing valve was opened and the water flowed through the test geometry. Figure 2-8 shows a top-down view of the test facility water subsystem and marks key components.

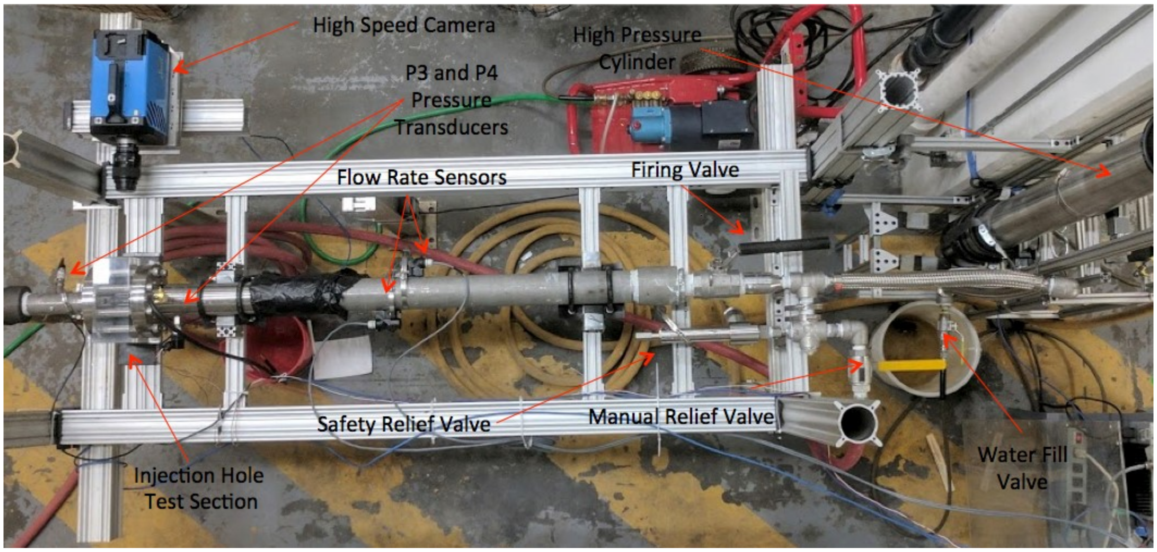

Figure 2-8: Top-down view of water subsystem.

In addition to the technical requirements, a few other design considerations were made for the water subsystem to decrease head loss, ensure proper sensor measurements, and safely isolate the system upstream of the test geometry while pressurizing the test facility. First, the pipe was expanded in steps from ½" NPT at the outlet of the high-pressure piston to a 36" long, Size 3 NPT pipe. The equation for head loss, with volumetric flow, is defined by,

$$H_L = \frac{8\rho f L\dot{V}^2}{\pi D^5} \tag{2-1}$$

By simple inspection of the equation, increasing pipe diameter (D) for the same volumetric flow rate ($\dot{V}$) results in a dramatic decrease in head loss. This pipe was also directly upstream of the test geometry, because its length was required for accurate flow rate measurements. According the manual for the flow rate sensor (Badger Meter 2016), the sensor must be placed 10x the inner diameter downstream of any changes to pipe diameter. Additionally, the pipe was sized larger than the upstream diameter of the test block, to prevent an expansion directly before it, which could cause flow separation from the pipe walls and affect the flow rate sensor measurements.

To safely isolate, drain, and prevent the water subsystem upstream of the test section from over pressurizing a series of valves were installed. These included a preset safety release valve rated for 2600 psig, a manual release valve, the water fill valve, the firing valve and the air escape valve. The water fill valve isolated the test facility from the house water during pressurization and testing. The firing valve isolated the water-side of the high-pressure piston from the atmosphere, which allowed for it to be filled prior to each experimental run. The air escape valve was left open during filling to allow for trapped air in the subsystem to escape, then closed prior to each run.

2.4 Nitrogen Subsystem

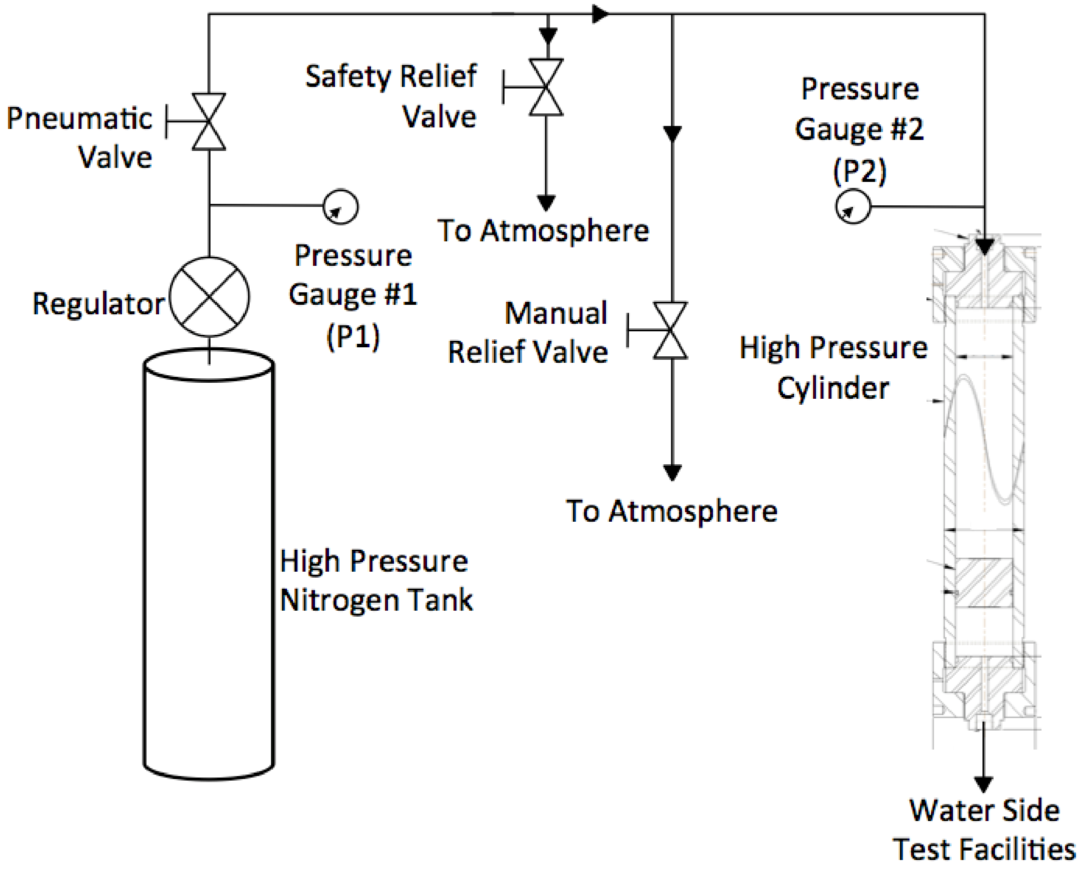

Figure 2-9: Schematic of test facility nitrogen subsystem.

The nitrogen subsystem, shown above, was defined by all the piping and associated components, which used nitrogen (N_2) as a working fluid. This supplied the test facility with high pressure that was used to drive water through the orifice plate. All pipes and fittings were initially rated for 5000 psig or above, but as modifications were made, this was lowered to 3000 psig. The modifications to the nitrogen subsystem will be described later in this section. The high-pressure source was a commercial nitrogen tank supplied by Air Gas; two different tanks were utilized over the course of the research. For lower pressure tests NI-300 tanks were used, which held N_2 at 2650 psig. For higher-pressure tests, NI HP6K tanks were used, which held N_2 at 6000 psig. It was determined the pressure inside of the nitrogen tanks needed to be at least double the desired tank regulator outlet pressure to provide consistent flow rates during experimental runs. This resulted in the need for the two different tank sizes for testing.

To control the flow rate and pressure out of the nitrogen tanks, a regulator was purchased, and then replaced after it was determined the initial regulator was causing dramatic pressure loss. For this test facility the final regulator was an Emerson 44-1300 Series venting regulator with a pressure input rating of 6000 psig, output rating of 2500 psig and a flow coefficient

(Cv) of 2.0. It was required to have a venting feature to safely release the nitrogen at the end of each experimental run.

In addition to the venting regulator, a series of valves were installed throughout the nitrogen subsystem for safety and as a trigger signal. Manual and automatic safety relief (rated for 4000 psig) valves, similar to those in the water subsystem, were used to prevent over pressurization of the nitrogen subsystem. They also were used to help drain the built-up pressure in the subsystem at the end of every experimental run. A pneumatic valve was also installed directly downstream of the regulator, where the electronic signal required to open and close the valve was used as trigger signal for the data acquisition system (DAS). The DAS will be described in detail in Section 2.6.3 Data Acquisition System.

As mentioned previously in this section, the nitrogen subsystem went through multiple modifications over the course of this experiment. These modifications were performed to decrease the head losses measured in the nitrogen subsystem. During initial testing, there was significant head loss. The pressure drop through the nitrogen subsystem alone was on the same order of magnitude as the pressure differential across the test geometry or above. Three major modifications were made to combat these losses; six feet of 0.25” diameter corrugated hose was replaced with 0.375” diameter stainless steel pipe, then the majority of the pipes in the subsystem were increased from 0.25” diameter to 0.375” diameter and, the regulator discussed above was installed. Referring back to Equation 2-1, for the same flow rates and pipe conditions, an increase in pipe diameter from 0.25” to 0.375” would result in a decrease of head loss by a factor of 7.6. With these three updates, the necessary flow conditions across the test geometry were achieved.

2.5 High-Pressure Cylinder

The interface between the water and nitrogen subsystems was a high-pressure cylinder manufactured by the High Pressure Equipment Company. To meet the technical requirements listed in Section 2.1, the cylinder had an internal volume of three gallons. This allowed for an approximate test duration of three seconds for the maximum pressure differential (2500 psid) at the test geometry. Also, to meet the initial safety requirements for the nitrogen subsystem, the piston was rated to 5000 psig.

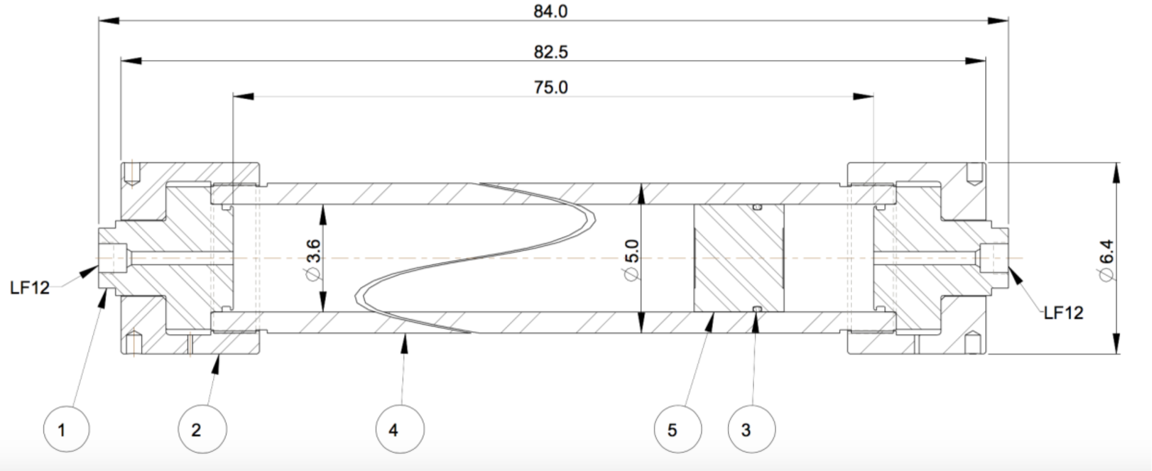

Figure 2-10: Dimensions of high-pressure cylinder.

The cylinder dimensions are shown above in Figure 2-10. Both end caps have a 0.4375" diameter with either a 0.25" or 0.5" NPT fitting to connect to the nitrogen or water subsystem respectively. Inside the cylinder is a 3" tall disc that acts as the piston. Again, conforming to the technical design requirements, every component was manufactured from stainless steel. The cylinder's orientation within the test facility is shown below.

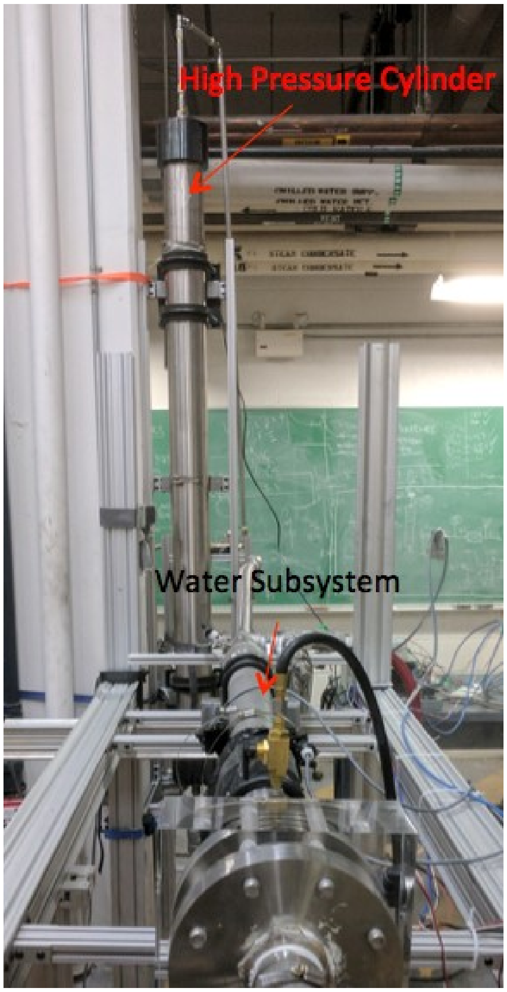

Figure 2-11: Vertical mounting of the high-pressure cylinder upstream of the water subsystem.

Due to the small openings in the end caps it was necessary to mount the piston vertically, shown in Figure 2-11. If the piston were horizontal mounted, air would become trapped inside it once the water level was above the openings in the end caps. This prevented the cylinder from completely filling and would have meant the test facility did not meet the test duration technical requirement. It is important to note that the head pressure supplied from the house water supply was sufficient to raise the piston. This was checked via calculations and confirmed by filling the piston, and then measuring the amount of water drained in the vertical configuration.

2.6 Data Acquisition System

The test data acquisition system (DAS) was comprised of all the sensors, data acquisition unit (DAQ), accompanying electrics, power supply, and high-speed camera required to collect the data for this thesis. The list of sensors includes four pressure transducers, one ultrasonic flow rate sensor, and a high-speed camera.

2.6.1 Pressure Transducers

Four pressure transducers were placed throughout the test facility to measure the static pressure at key locations. The name, location, type, and pressure rating of each pressure transducer are summarized in the table below.

Name	Location	Type	Rating (psi)
P1	Regulator Outlet	Gauge	5000
P2	Upstream of High-Pressure Cylinder	Gauge	3000
P3	Upstream of Test Section	Gauge	3000
P4	Downstream of Test Section	Absolute	100

Table 2-2: Summary of pressure sensors.

In Figure 2-7 and Figure 2-9 the locations of the pressure transducers are shown. These locations were selected so pressure losses throughout the test facility could be measured and, if necessary, provide insight into areas where modifications would be necessary to decrease head loss. Also, it should be noted that the P3 transducer was labeled as a gauge type transducer; however, it was determined as an absolute type transducer. To account for this, 14.7 psig was subtracted from the measured pressure during post processing.

2.6.2 Flow Rate Sensor

To measure the volumetric flow rate through the water subsystem an ultrasonic flow rate sensor was installed. The specific model was a TFXL Ultrasonic Transit Time Flow Meter from Dynasonic. This sensor was selected as the technology allowed for a non-invasive flow rate measurement, opposed to a normal pitot tube, which must be inserted into the flow. The sensor was comprised of two separate components, a base unit and two transducers.

The transducers were mounted to the water subsystem pipe and then connected to the base unit. Specifically, the transducers were horizontally mounted on the Size 3 stainless steel pipe just upstream of the test geometry. The transducers exact location was 28.5” upstream of the test section and 29” downstream of the firing valve with a spacing of 1.83” between them. This location met the requirements from the Badger Meter manual (2016).

The sensors functioned by sending ultrasonic sound waves between the two transducers. The sound waves moving with the flow (in the downstream direction) traveled faster than the sound wave moving against the flow (upstream direction), and resulted in a time delay. This delay was measured and used by the base unit to calculate the volumetric flow rate within the pipe.

The base unit outputted two different signals, one through a USB-A connection that was read by the Dynasonic software called ULTRALink Utility, and the second was a 4-20 mA current signal. The associated maximum and minimum flow rates could be set via the ULTRALink software. Due to the DAQ, being configured to only measure voltage signals, a 249 Ω, 1 W resistor was placed in parallel to the 4-20 mA signal to produce a corresponding 0-5 volt signal.

In addition to acting as an interface to measure the flow rate, the ULTRALink Software was used to calibrate the sensor itself. This calibration included configuring the sensor to measure more transient conditions, which would occur during higher-pressure experimental runs.

Even with assistance from SME's from Badger Meter, there was still a delay between the flow rate signal and pressure transducer signals. The delay varied, but was consistently on the order of a few seconds. This delay resulted in the sensor not measuring maximum flow rates during the steady state portions of the higher-pressure experimental runs due to the shorter test durations. A solution was found, and will be covered in the experimental methods section.

2.6.3 Data Acquisition Unit and Circuit

All of the sensors used for this research were connected to a 16-channel analog input DAQ, which was controlled via LabVIEW software. The specific DAQ model used was NI USB-6210 and manufactured by National Instruments. The DAQ was configured to receive voltage differential signals up to 10 V. In addition, a triggering and power circuit, shown below, was built to provide the proper excitation voltages to all the sensors and the pneumatic actuator.

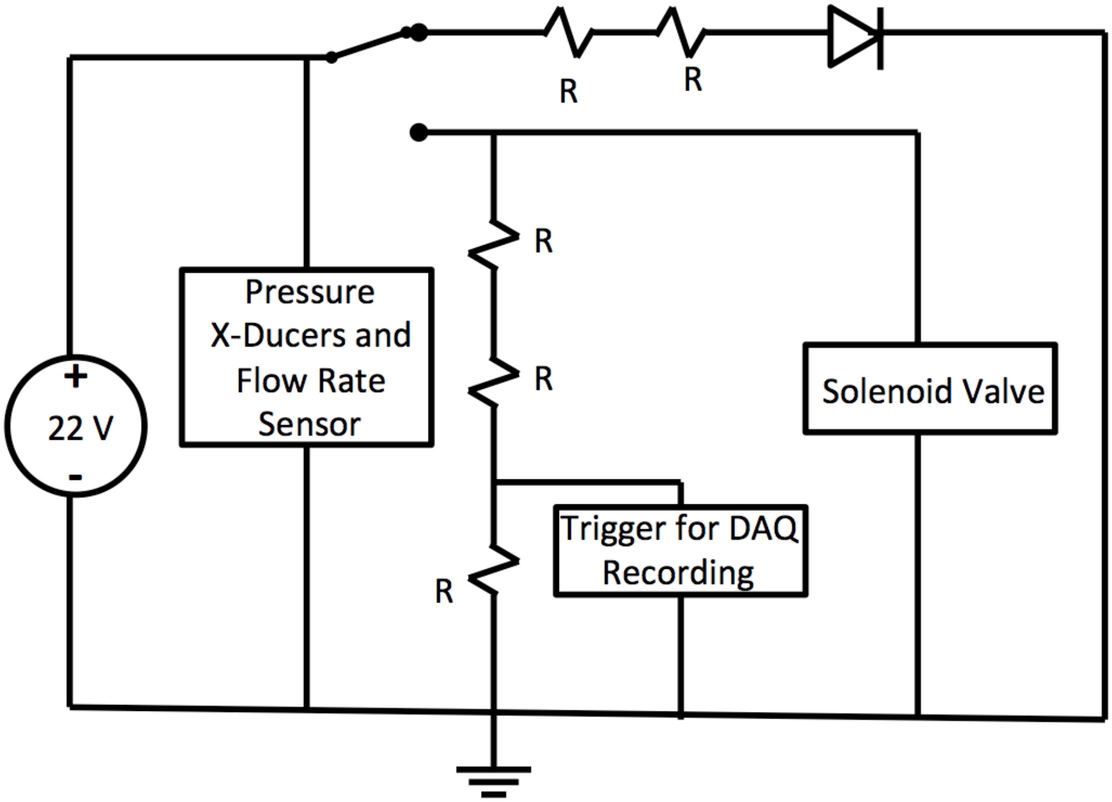

Figure 2-12: Control circuit for test facility.

The circuit provided a trigger signal that was sent to the DAQ once the switch was flipped. This signal was used by the data collection software (LabVIEW) to trigger the start, and end of data collection for each experimental run. The switch on the circuit board also opened, and closed a solenoid valve that operated the pneumatic valve in the test facility's nitrogen subsystem. This triggering method ensured the entire test event was captured.

2.6.4 High-Speed Camera

In concurrence with the technical requirements, a high-speed camera, shown below, was installed in the test facility to detect the onset and presence of any phenomena occurring in the test geometry during an experiment. For this research a pco.dimax camera was installed in the test facility to record video that was focused on the throat of the test geometry.

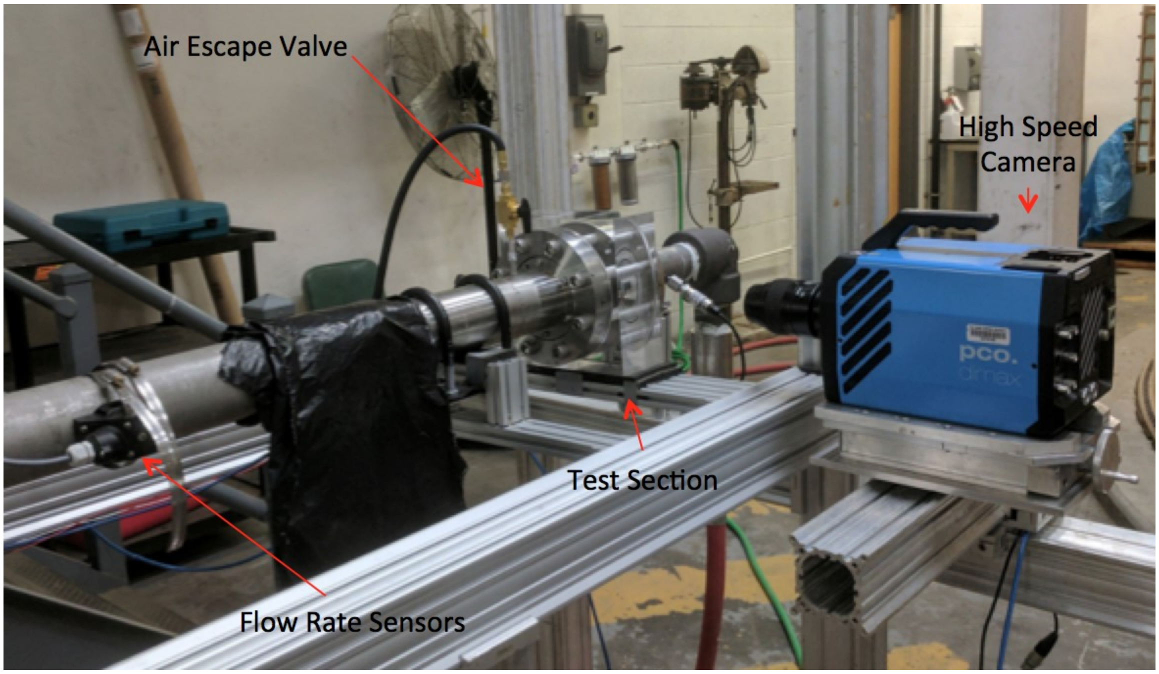

Figure 2-13: High-speed camera.

A 105 mm Nikkor lens was used to zoom in on the test section throat. The camera was positioned such that the images, an example is shown below, captured the upstream and downstream flow conditions, and the flow through the throat for each experimental run.

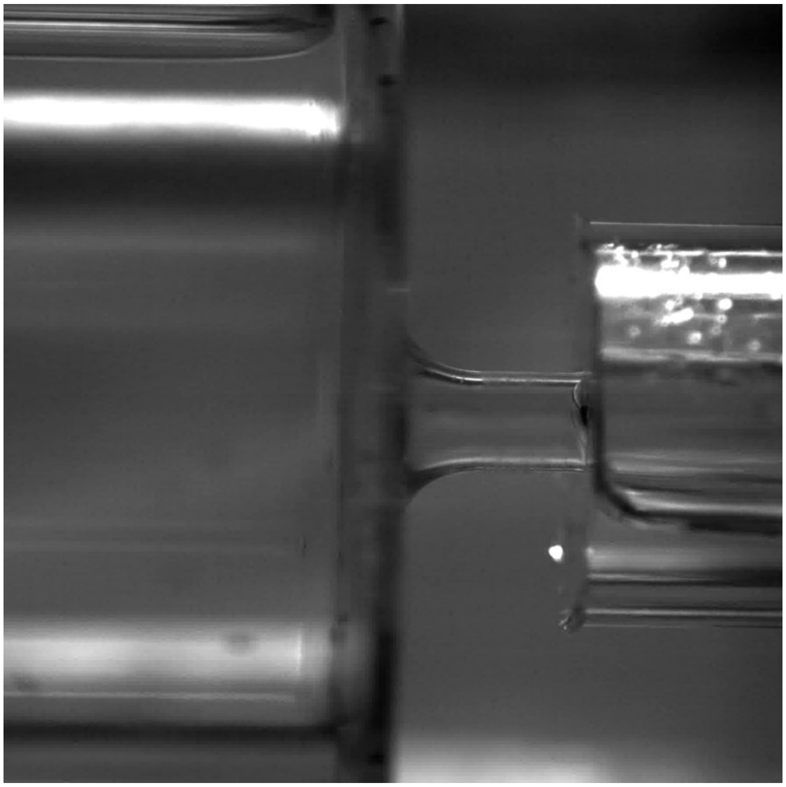

Figure 2-14: Sample image from high-speed camera.

3 Experimental Method and Analysis

This section details the methods implemented to characterize the test geometry discharge coefficient, $C_{d,TS}$, derived from pressure differential comparisons across the test facility. Additionally, it includes supporting analysis from high-speed video recorded during each experimental run. The methodology provides an overview of the procedure performed for each test and the processing required to determine the steady-state data, which was used to determine the orifice discharge coefficient. Further analysis was performed to calculate the average discharge coefficient, Reynolds number and cavitation number for each test as well. All high-speed video was exported and analyzed to determine the presence of any fluid phenomena.

3.1 Experimental Procedure

At the start of each experimental run, water was pumped through the test facility's water subsystem, this was done to remove any excess particulate that accumulated in the pipes which were not filtered out previously. This "flushing" also began to fill up the water subsystem for the start of an experimental run. Once the water began to drain from the air escape valve at the top of system the valve was closed. The firing valve was closed promptly after. Closing this valve isolated the water-side of the high-pressure cylinder from atmosphere, allowing it to be filled, and minimized the amount of air trapped inside the water subsystem. Nevertheless, air was still trapped inside the high-pressure cylinder due to it not having a release valve. It was extremely important to minimize the amount of air in the subsystem, as the air bubbles could cause local variations in the flow. These variations could induce error into the analysis calculations.

Once the cylinder was filled, the house water supply was shut off and the test facility water fill valve was closed. This process isolated the water subsystem from atmosphere, except for the downstream side of the test section. The nitrogen subsystem was then isolated from atmosphere and pressurized. The pressurization of the subsystem was tracked via the LabVIEW software.

After the test facility was pressurized to the desired pressure, the electronic trigger switch was turned on to start data collection. Immediately afterward, the high-speed camera began recording and the firing valve was opened. Although the camera and firing valve were not electronically synchronized, both started at approximately the same time. It was not necessary to synchronize them because the video settings allowed for an entire experimental run to be captured. Additionally, it was not possible to confidently predict the amount of time for steady-state conditions to occur after the firing valve was opened. If the camera was configured for extremely high frame rates there was a possibility of not recording the flow during steady-state conditions. This was because the increased frame rates would decrease the total time of the recording.

After completing an experimental run, the test facility was depressurized. The sensor and video data were saved using the LabVIEW and Camware software respectively.

3.2 Initial Data Processing

Once the raw data was recorded, initial processing was done to convert the voltage signal to pressure and flow rate. Additionally, all non-test data was excluded and a Butterworth low-pass filter was applied.

3.2.1 Initial LabVIEW Processing

Before the data was filtered or heavily processed to determine discharge coefficients, there was some initial processing performed in the LabVIEW software. The raw data outputted by the sensors was converted to pressures (psig) and flow rates (GPM). For the pressure transducers, scaling equations were used which were determined from data provided by their respective calibration sheets. For the flow rate sensor, the minimum and maximum output current signal, which was converted to a voltage via a resistor, could be set to correspond to user-defined minimum and maximum flow rate. For this test facility, those values were 0 and 95 GPM.

3.2.2 Non-Test Data Removal and Filtering

To ensure data was collected during steady-state conditions for each run, the data collection software was started during the pressurization of the nitrogen subsystem and ended after all the water was expelled from the water subsystem. This process resulted in the collection of multiple seconds of non-test data. To remove this data, a minimum pressure threshold of 25 psig was set for the P3 pressure transducer, located just upstream of the test geometry. This sensor was selected for two reasons:

1. Prior to the opening of the firing valve, which initialized the start of each experimental run, P3 would be at atmospheric pressure; therefore, a pressure increase to 25 psig would only be due to the start of an experimental run.
2. For lower-pressure tests, it was not assumed there would be a significant pressure rise in the P4 sensor, downstream of the test section during an experimental run.

Once the non-test data was removed, high-frequency noise was removed using a first-order Butterworth low-pass filter with a cutoff frequency of 10 Hz. This filter was applied to all four pressure sensor data sets as well as the flow rate sensor. By doing this, the associated delay due to the filter would appear in all the data sets, and subsequently, each data channel would remain synchronized to the others. As a result, no time shift was applied to the sensors to correlate the data in time. The filter caused a time delay between the video and sensor data, however, as the camera was not synchronized with the pressure sensors, this delay not an issue.

3.3 Video Processing

For each experimental run high-speed video was recorded and required processing so it could be in an easily analyzable format. To do this, the manufacture-supplied software, Camware, was used. This same software was also used to initialize and run the camera during each run. The processing of each video file included an initial review of the footage to manually adjust brightness and improve contrast of the image. Once this was complete the entire video file was exported to ensure no loss of data. The output frame size was set to match the frame size of the video file, which was either 1776x1532 or 1776x1776 pixels. The frame size was increased to show a small air pocket that sometimes formed at the top of the inlet section of the test geometry, prior to the throat. Additionally, each raw file was exported at 30 fps opposed the raw recording rate which was either

480, 600, or, 720 fps. This decreased frame rate allowed for the final video to play at 1/16th, 1/20th, and 1/24th the speed of the real-time event. The videos showed "shaking" at the beginning and end of each run, this correlated to the opening of the firing valve, and the piston reaching the bottom of the high-pressure cylinder respectively. These events were used to correlate the pressure data to the video data. Finally, screen captures of the video were taken for the purposes of documentation.

3.4 Steady State Definition

To ensure an accurate discharge coefficient was calculated for the test geometry, only data captured during steady state conditions could be used. For these experiments that meant the volumetric flow rate of the water did not change with time. Initially, it was assumed the flow rate sensor would provide the time range for each test when there were steady-state conditions. Though, it was discovered there was a multiple second time delay between the flow rate sensor data and the pressure data. This delay was due to the design of sensor, which will be discussed further in this section. As a result, another method of identifying steady-state conditions (and ultimately flow rate) was determined.

3.4.1 Pressure Differential Comparisons

Based on Equation 1-5 (flow rate based on pressure) it can be shown that the volumetric flow rate of a fluid is proportional to the square root of the pressure differential between two points.

This observation was the basis of the steady-state conditions used in this analysis. Comparing the pressure differential between P2 and P3 (ΔP23), which represented the flow rate through the pipes of water subsystem, to the pressure differential across the test section, P3 and P4 (ΔP34), provided a good indication that the flow rate had reached steady-state conditions throughout the entire water subsystem. More specifically if the difference between the two pressure differentials, ΔP23 and ΔP34, now referred to as PSS (for steady-state), remained constant with respect to time, the experiment had reached steady-state conditions. P2, which was in the nitrogen subsystem, was just upstream of the high-pressure cylinder. For the purposes of this analysis it was assumed the pressure inside the cylinder was also the pressure at P2 and therefore at the beginning of the water subsystem. This assumption was shown to be reasonable and is detailed in Appendix B.

3.4.2 Steady-State Threshold

To determine the timeframe during each run when the experiment was in steady-state conditions, or when Pss≈0, a numerical derivate was calculated. To help remove some of the “noise” associated with numerical derivatives, PSS was smoothed using a 100 sample moving average, this correlated to 0.1 second of data being averaged at a time. For this analysis a 2nd-order central difference formula was implemented (Moin 2012). The formula is shown below:

$$\frac{dp_j}{dt} = \frac{p_{j+1} - p_{j-1}}{2\Delta t} \tag{3-1}$$

Next, a maximum threshold magnitude of the numerical derivative was determined based on review of all the experimental data collected, and is show below. The units are psid/s.

$$||\frac{dp}{dt}|| \leq 250 \tag{3-2}$$

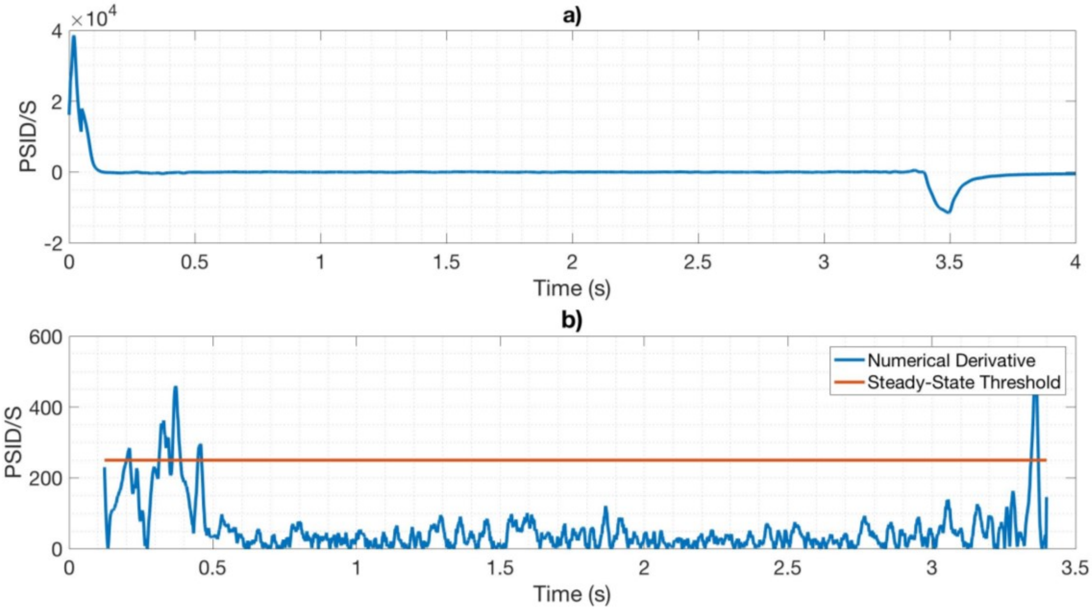

Figure 3-1: a) PSS numerical derivative for duration of a sample experiment. b) PSS numerical time derivative during the steady-state phase of a sample experimental run with numerical threshold of 250 psid/s.

Figure 3-1b, shown above, compares the threshold with the absolute value of the numerical derivative for an example run. All data below the threshold was considered to be steady state. The reason for the non-zero threshold value is due to the inherent noise in the numerical derivate, and while the noise can be decreased through smoothing of the data, not all was removed. Additionally, from Figure 3-1a it is clear this threshold value is approximately zero when compared to the values of the derivatives at the beginning and end of a run.

3.4.3 Additional Considerations

While the condition described above provided a sufficient threshold to define the steady state times for each run, it did not remove all pressure fluctuations in the data, specifically at the end of the run. It is believed, the pressure oscillations at the end of each run were due to the release of compressed air bubbles trapped in the high-pressure cylinder. This data was removed because the high-speed video showed the air pockets taking up a significant volume in the throat of the test geometry during a run. This phenomenon could result in variations of the fluid properties and could affect the discharge coefficient calculation. Below is Figure 3-2 showing the air bubbles in the test geometry at the end of an experimental run.

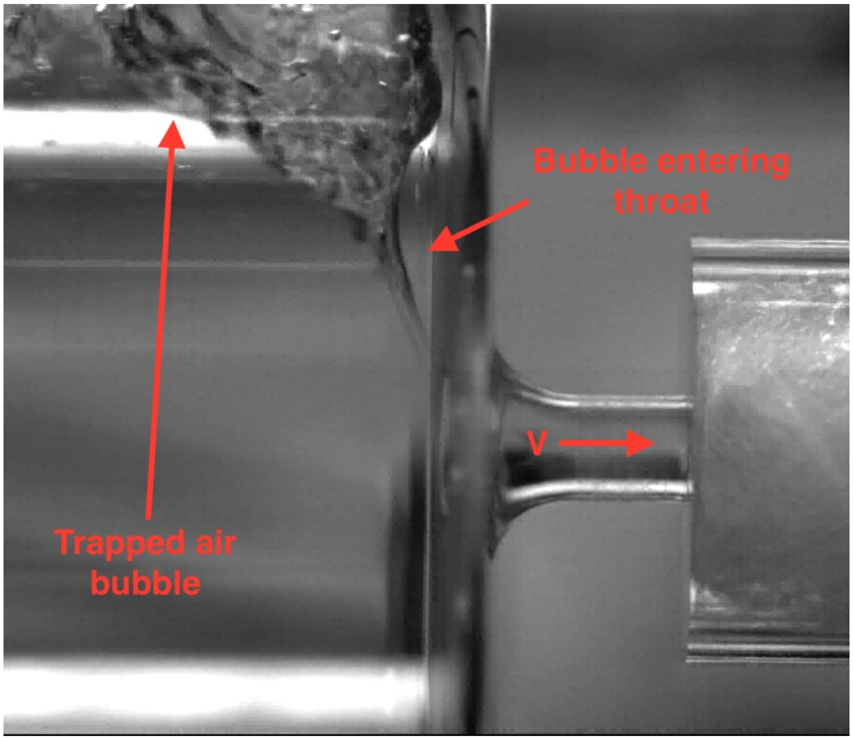

Figure 3-2: Trapped air bubble entering throat of test geometry.

3.5 Flow Rate Sensor

As mentioned in the previous section, there was a delay in the flow rate measurement on the order a few seconds for each run. This delay occurred even after reconfiguring it to increase response time based on the recommendations from the sensor manual (Badger Meter 2016). The delay posed a significant issue when calculating the test geometry discharge coefficient for higher-pressure runs because the run could end before the flow rate sensor measured a steady-state flow rate.

For lower-pressure runs, which ran for approximately 10 seconds or longer, the steady-state data was still collected from the flow rate sensor. This was confirmed by comparing the calculated ideal flow rate from the pressure sensors to the measured flow rate from the flow rate sensor. Figure 3-3 shows the steady-state flow rate from the flow rate sensor and the ideal flow rate based on pressure differential. The flow rate sensor data was shifted earlier in time by ~3.5 seconds to compare the similarities between the two curves.

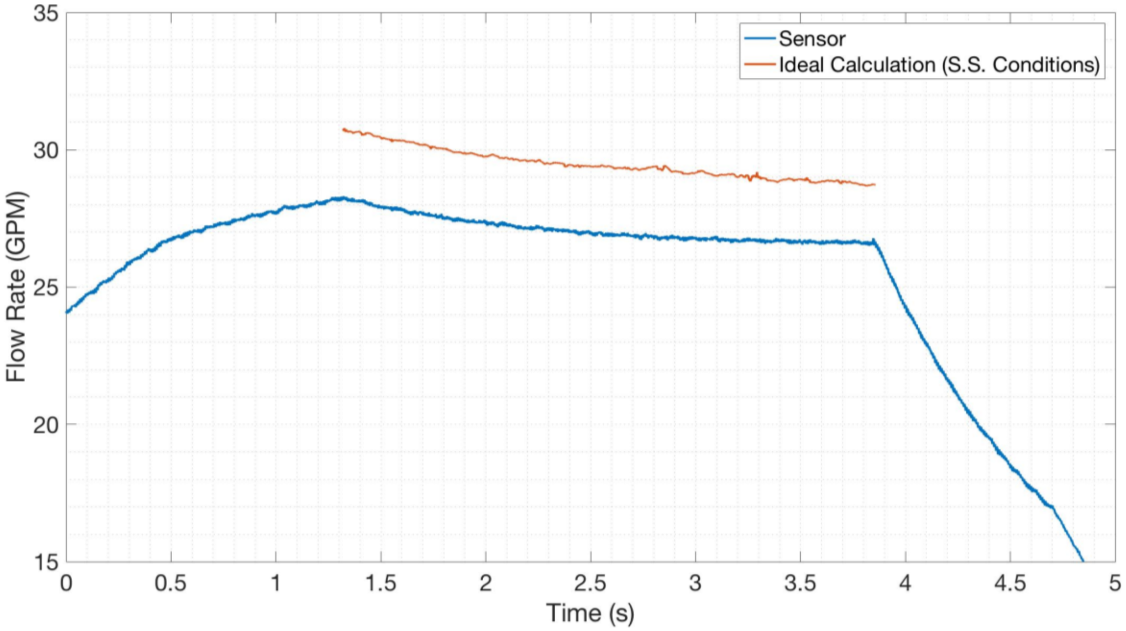

Figure 3-3: Comparison of measured flow rate from flow rate sensor to steady-state flow rate calculated from pressure transducers.

The only difference between them is the magnitudes, which was expected as the calculated flow rate is ideal while the measured flow rate accounts for real world losses. It was found that for eight of the low-pressure runs, the flow rate sensor data correlated well with the ideal calculated flow rate.

3.6 Water Subsystem As A Flow Rate Sensor

Due to the flow rate sensor not consistently measuring steady state flow rates another approach was required to determine the actual flow rate through the test geometry. While determining steady state conditions it was realized that the entire water subsystem upstream of the test facility acted like a flow rate sensor, and this fact was exploited to determine the actual flow rate through the system. This was done by correlating the calculated flow rate, based on $\Delta P23$, to the measured flow rate sensor for those eight experimental runs. An average water system discharge coefficient ($C_{d,H20}$) of 0.016 was calculated for the water subsystem; however, there was no way to confirm if this value was reasonable based on theory as the there was no analogous orifice design and accompanying discharge coefficient. This low value was due to using the actual diameters at P2 and P3 respectively.

To verify the accuracy of the coefficient, it was assumed the end cap of the high-pressure cylinder on the water subsystem side acted like a sharp-edged orifice plate flow meter. This type of orifice has a known range of values for the discharge coefficient. By confirming the cylinder discharge coefficient ($C_{d,Cyl}$) agreed with expected coefficient values for the eight experimental runs used to determine $C_{d,H20}$, the water subsystem discharge coefficient could be assumed to be correct.

3.6.1 Cylinder Discharge Coefficient

As stated above, the end cap of the cylinder (its cross-section is shown in Figure 3-4below) resembled the geometry of a sharp-edged orifice flow meter.

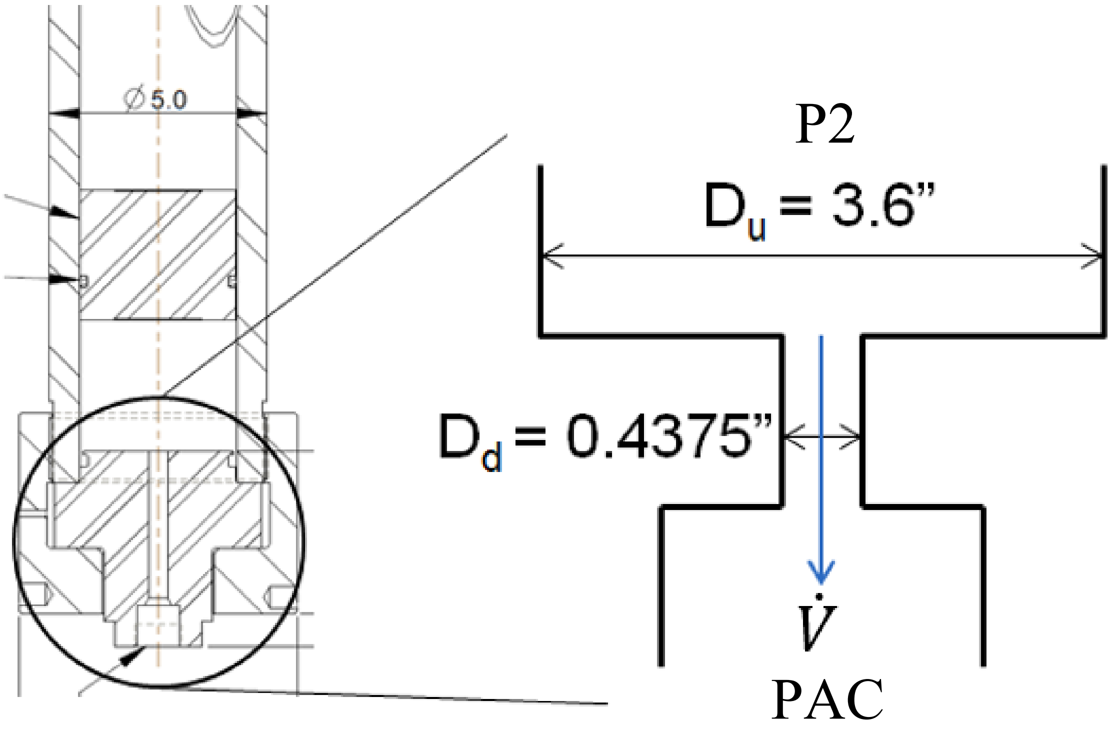

Figure 3-4: Cross-section of end cap geometry for high-pressure cylinder.

These types of flow meters have been researched extensively as well as their discharge coefficients, which typically center on 0.62 (Kundu et al.

2012) for similar values of β. To calculate the discharge coefficient for the cylinder, $C_{d,Cyl}$, the pressure inside the cylinder was assumed to be P2. This assumption was verified and is shown in Appendix B. Additionally, the pressure just after the high-pressure cylinder (PAC) was also needed.

To estimate the pressure in the water subsystem just after the high-pressure cylinder, PAC, head loss calculations were performed. Starting from P3, and moving upstream, the head loss associated with each component was determined until just downstream of the cylinder, resulting in an estimate for PAC. The calculations are captured in Appendix B, but key assumptions, equations, and components are detailed in the Introduction and below.

Initially, it was assumed that the fluid was incompressible, and because the flow was at steady-state conditions, Bernoulli's equation with head loss could be used to estimate the upstream pressure. Equations 1-1 and 1-3 show steady-state Bernoulli's equation and the head loss equation respectively

To calculate the friction factor, f, for the head loss from P3 back to PAC, Equation 3-3, Blasius' Approximation, shown below, was used (Frank White 2005). It is accurate for Reynolds numbers between 4000 and 10^5.

$$f_{Blasius} \approx \frac{0.0791}{Re^{0.25}} \tag{3-3}$$

To calculate the Reynolds number, the ideal flow rate across the test section was used. The ideal flow rate was used opposed to the actual measured flow rate, from the flow rate sensor, because during the analysis the measurement could not be assumed to be accurate yet. Using this approach for determining Reynolds number however caused the Blasius Approximation to under-predict the friction factor by 2.7%. This result was based on the difference between the ideal and actual flow rates through the test geometry, which themselves differed by approximately ~10%.

Additionally, there was five feet of flexible corrugated hose between the high-pressure cylinder and P3 measurement location. The head loss for it was calculated based on pressure drop plots provided by the manufacture. These plots estimated the pressure drop per foot of pipe for a given flow rate and are shown in Figure 3-5 below.

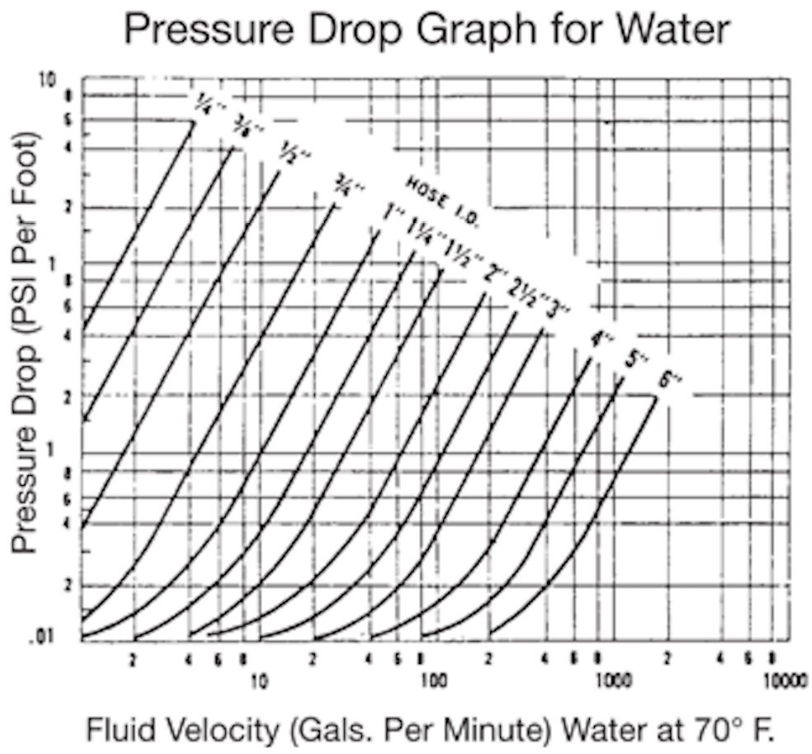

Figure 3-5: Plot of pressure drop per foot of hose of corrugated hose for varying diameter (Hose Master 2017).

Based on this plot a power law equation for head loss was interpolated for 1" diameter hose. The equation is shown below, and has an R^2 value of 0.99641, indicating a very good fit of the data.

$$\Delta P = 0.0018(FR_{GPM})^{1.77} \tag{3-4}$$

The reason for determining $C_{d,Cyl}$, then only using it verify the flow rate measurement for low-pressure runs, was because there was induced error in the head loss calculation, which is ~10% (Pritchard 2011). Directly determining $C_{d,H20}$ from the flow rate measurement induced no additional error which would carry over to the test geometry discharge coefficient,

$C_{d,TS}$. The fact that there was up to 10% error in $C_{d,Cyl}$ was accounted for when determining which low-pressure runs had accurate flow rate measurements. If the $C_{d,Cyl}$ value was within 10% of the expected mean, or between 0.56 and 0.68, it was assumed the flow rate measurement was accurate.

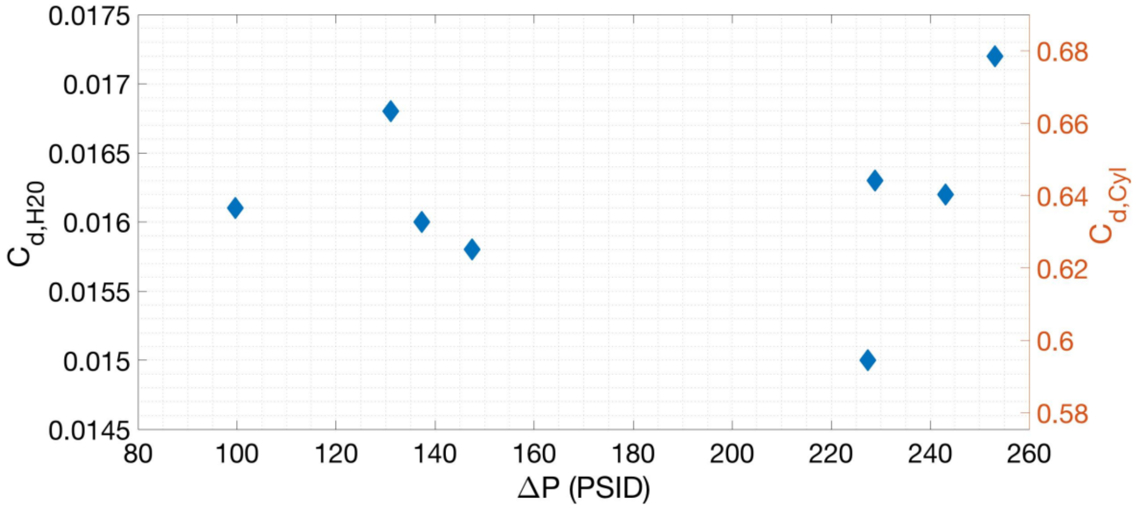

Figure 3-6: Comparison of $C_{d,H20}$ vs. $C_{d,Cyl}$ for the eight low-pressure experiments that showed good quality flow rate sensor data. The left-side axis shows the water subsystem discharge coefficients, while the right-side axis shows the corresponding cylinder discharge coefficients for the same experiments.

Figure 3-6 shows that the discharge coefficient fluctuated very little for those eight runs. Also there was no clear relationship that can be extrapolated for higher-pressure runs, so the individual $C_{d,H20}$ values for all runs were averaged together to determine a final $C_{d,H20}$ value.

3.7 Test Geometry Discharge Coefficient

Once the discharge coefficient for the water subsystem, $C_{d,H20}$, was calculated, the actual flow rate for all experimental runs was determined. This meant the discharge coefficient for the test geometry could be calculated. To do this, the ideal flow rate, based from the pressure across the test geometry ($\Delta P34$), was calculated using Equation 1-5.

Next, the test geometry discharge coefficient, $C_{d,TS}$ was determined for each test based on Equation 1-7.

3.8 Uncertainty Analysis

Uncertainty is inherent in all experiments; however, it can be approximated to provide a level of confidence in experiment results. In this section, major sources of uncertainty have been identified and their effects estimated to provide an overall uncertainty associated with the test geometry discharge coefficient.

The first source of uncertainty was from the sensors. Two different manufactures of pressure transducers were used, Omega and Wika. The measurement uncertainty for both sensors was 0.25%. Additionally, the measurement for the flow rate sensor was 1%.

The next source of uncertainty was due to variation in the flow rate during steady state conditions. For Bernoulli's equation, it was assumed that the entire water subsystem had reached steady state flow rates. However, because the steady condition was $\|dP/dt\| \leq 250$ psid/sec, the flow rate would vary slightly during the timeframe. To account for this, the percent pressure variation was determined, which is shown in Equation 3-5 for general terms.

$$\Delta x_{avg} = \frac{\sigma}{\sqrt{N}} \tag{3-5}$$

Where Δx_{avg} is the mean uncertainty of some value x, N is the number of samples, and σ is the standard deviation.

Another source of uncertainty was due to the variation in the discharge coefficient of the water subsystem, $C_{d,H20}$. This was determined by applying Equation 3-5 to the $C_{d,H20}$ data, which resulted in an uncertainty of 1.4%. In addition to this uncertainty the under prediction of the friction factor from Blasius' Approximation was included, which was 2.7%.

Finally, all sources of uncertainty were combined using the residual sum of squares method, which for a general case is shown below. This method assumes no correlation between each error source.

$$\Delta x_{total} = \sqrt{\sum \Delta x_{avg,l}} \tag{3-6}$$

This method resulted in a total average uncertainty of 3.2% for the test geometry discharge coefficient, $C_{d,TS}$.

4 Results and Discussion

This section presents the results and discussion of the test geometry discharge coefficient characterization and performance. It includes results from both the pressure data and the high-speed video. The experimental runs conducted were for pressure differential ranges across the test geometry between 65 and 1200 psid. The tabulated results for each experimental run can be found in Appendix C. Additionally, the overall performance of the test facility is discussed as it was designed and built for the experiment. To reiterate, the test geometry refers to the acrylic block and orifice geometry housed inside it.

4.1 Test Geometry Performance

The pressure transducer data provided the basis for determining the test geometry performance for the 59 experimental runs, while the high-speed video captured qualitative data to provide insight into the phenomena occurring within the test geometry during each run.

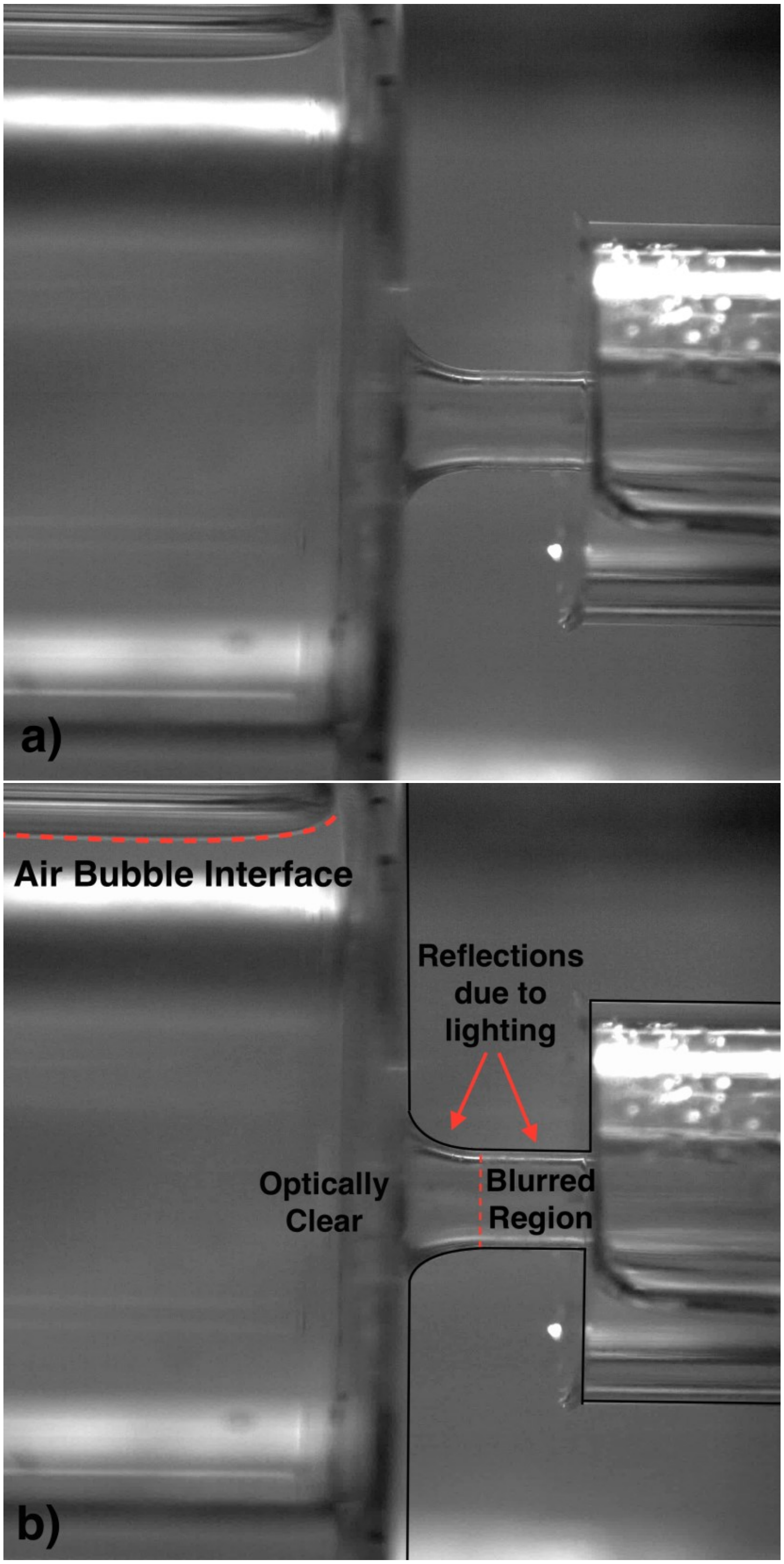

Figure 4-1: a) Raw image of fully flooded test section. b) Highlighted features of flooded test section with physical orifice geometry outlined in black.

Figure 4-1a, above, shows a raw image of the test geometry fully flooded with water. Figure 4-1b, highlights the features of the test geometry and identifies a few observations for discussion. There were reflections within the throat due to the lighting conditions during testing. In the throat of the geometry there was also a discontinuity in the surface finish, marked by the red dotted line. Blurring of the lighting reflections in the throat helps to show the change in the surface finish, and it is clearer in images during an experimental run. Again, this discontinuity was due to issues in polishing the straight portion of the throat. As a result, only the curved upstream portion of the throat could be smoothed until optically clear. The impact of these complications are discussed later in this section. The air bubble trapped in the upstream section of the test section is also highlighted.

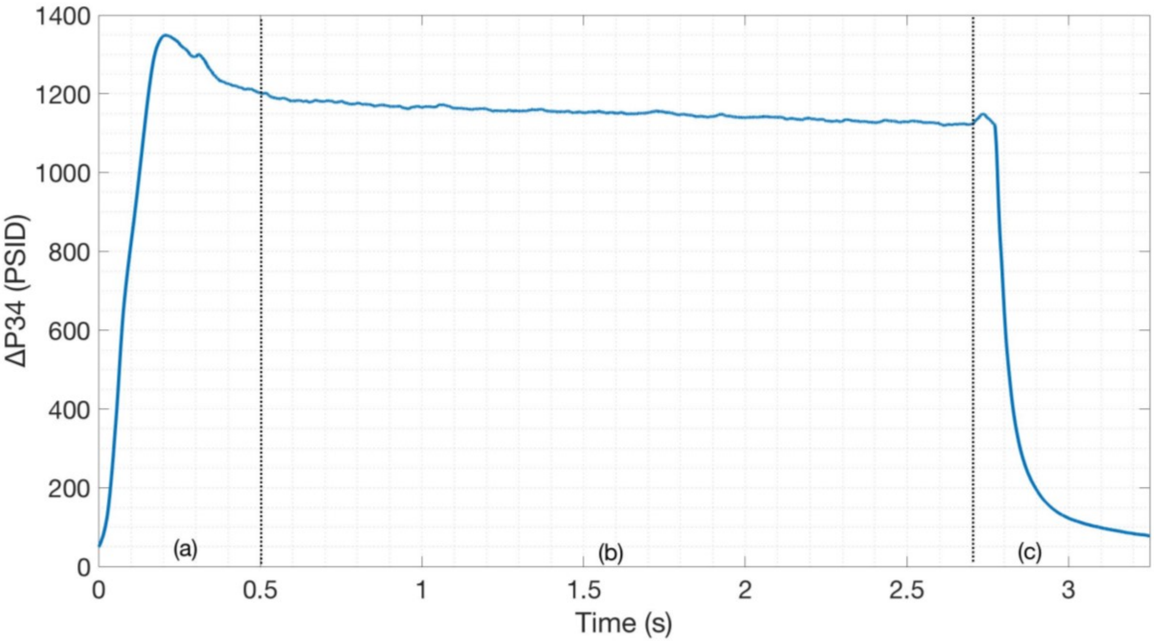

Figure 4-2: a) The initial phase of an experiment, when the test section is being pressurized. b) Steady-state phase where pressure and flow rate remain approximately constant c) end phase of the experimental run where test facility is depressurizing.

In Figure 4-2, the filtered pressure differential across the test geometry (ΔP34) for an example experimental run is shown. Each run was broken down into three major sections, (a) the initial transient phase, (b) the steady-state flow phase, and (c) the end of the experimental run. The data from the steady-state flow phase was used to evaluate the test geometry performance, since it was an assumption to accurately calculate flow rates from Bernoulli’s equation.

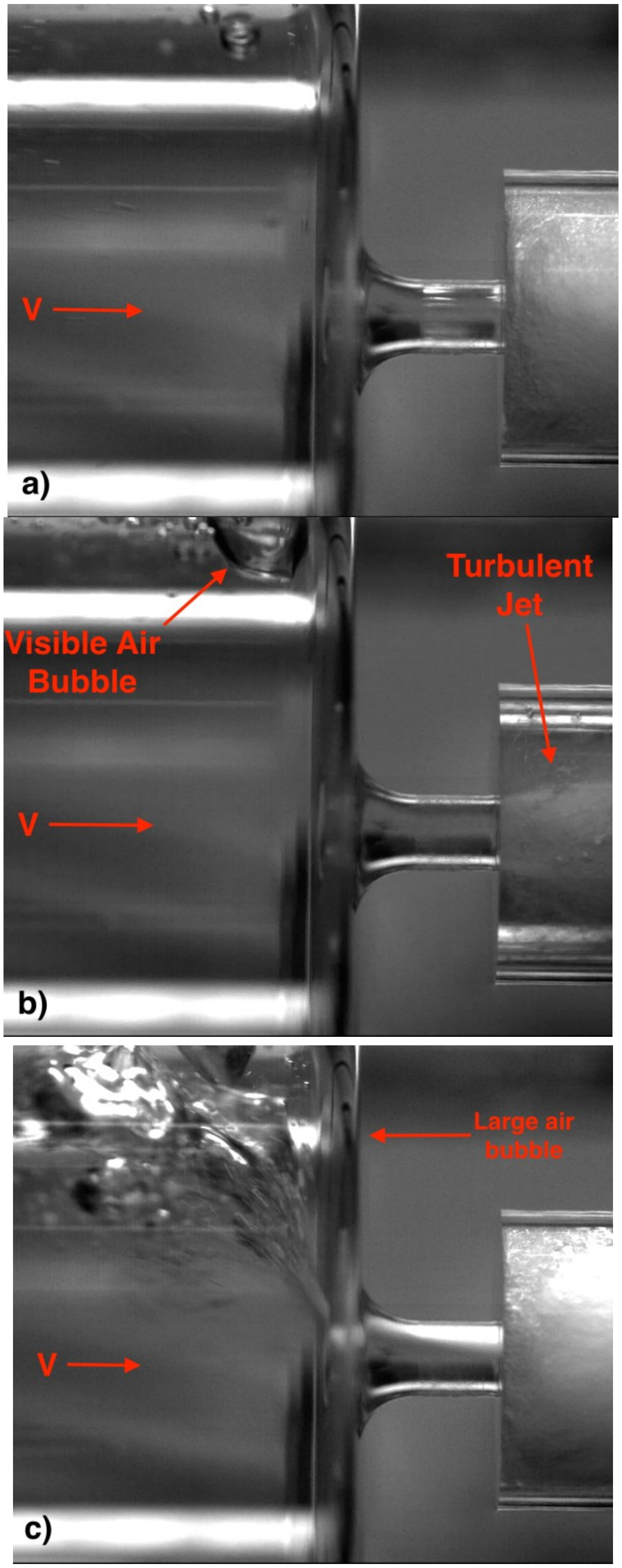

Figure 4-3: Images of three phases of low-pressure experimental run, a) initial pressurization, b) steady-state flow rate, c) end of steady-state flow rate and depressurization of test facility.

Figure 4-3 shows images captured during each phase of an example experimental run. During the initial phase (a), the downstream section of the test geometry showed a fully turbulent and chaotic structure containing bubbly flow, which filled the entire geometry. This was caused by large air bubbles trapped in the water subsystem at the beginning of the run that flowed through the throat of the test geometry. Also visible in (a) is the effect the discontinuity of the surface finish had on the clarity of the image.

Once the experimental run reached steady state (b) the air bubble concentration and size dropped and an opaque turbulent jet can be seen downstream of the throat. While the concentration of bubbles decreased during steady state, a small air bubble was visible during some of the smaller Reynolds number tests just upstream of the throat. It was always located at the top of the test geometry. Additionally, at the end of the test (c), a large air bubble became visible just upstream of the throat, which then entered the throat. This air bubble was from air trapped in the high-pressure cylinder during the filling of the water subsystem finally exiting the cylinder. The effect of the bubble can be seen in the pressure data.

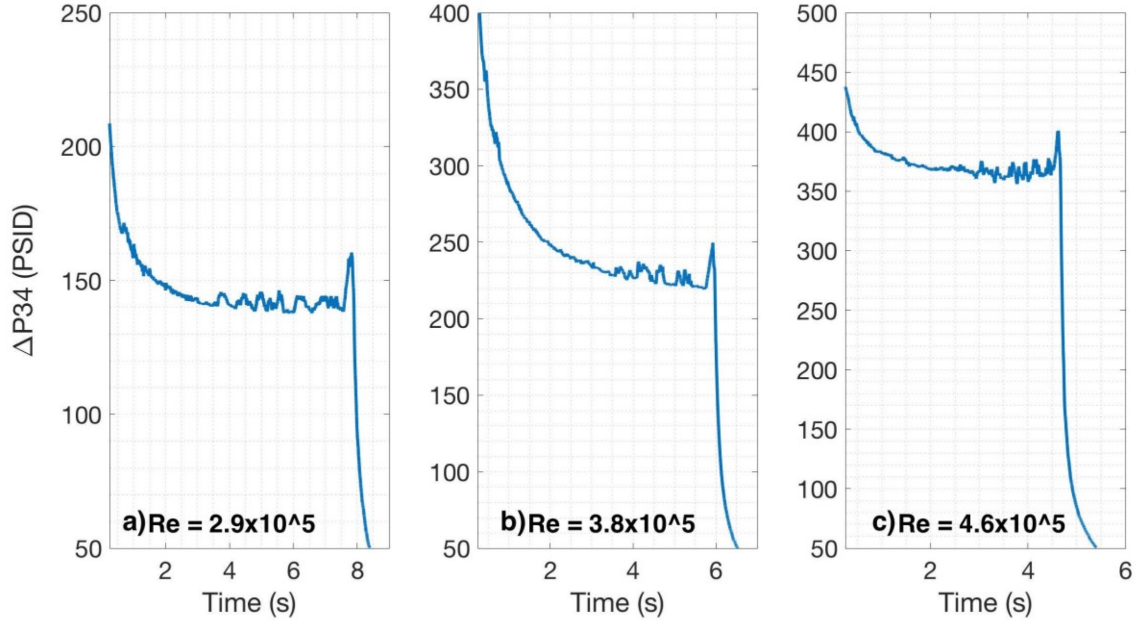

Figure 4-4: Oscillations in differential pressure across test geometry (ΔP34) for lower Reynolds number runs toward the end of the test due to trapped in high pressure cylinder escaping.

Figure 4-4, above, shows ΔP34 from three different low Reynolds number experimental runs. Each shows that during the end of the steady-state portion of the run there were pressure fluctuations. As mentioned in the Experimental Methods section, this portion of the pressure data was smoothed or not included when determining the test geometry discharge coefficient $C_{d,TS}$

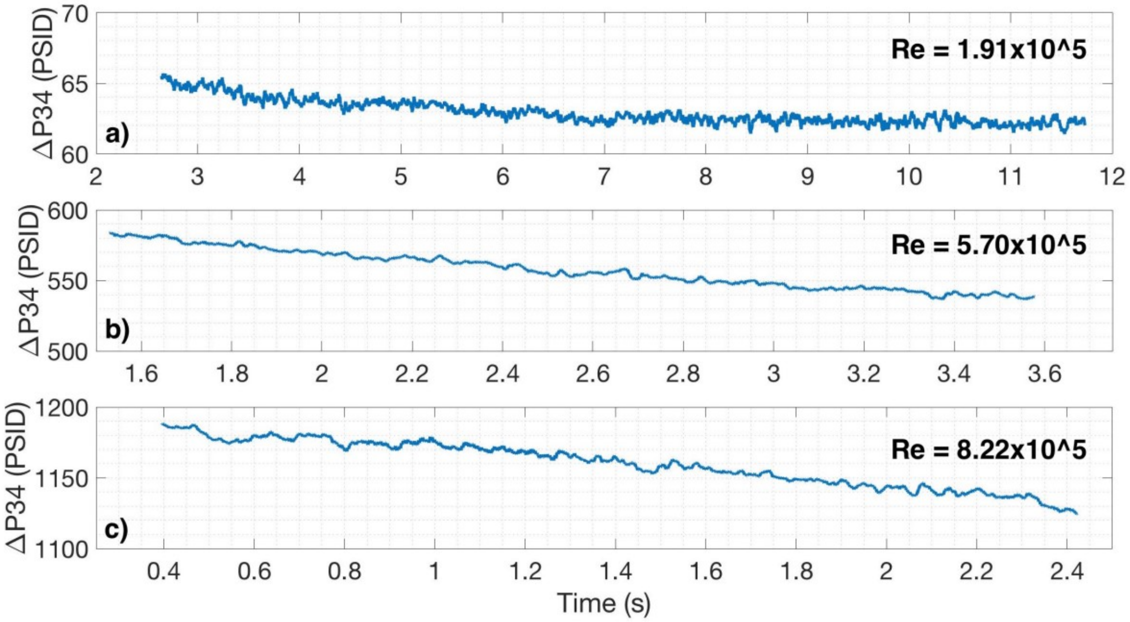

Figure 4-5: Steady-state pressure differential across test section (ΔP34) for different experimental runs at a) Re = 1.91x10^5 b) Re = 5.70x10^5 c) Re = 8.22x10^5.

Figure 4-5, above, shows a comparison between various runs at different Reynolds numbers. This figure highlights the similarities and differences between the overall shapes of the steady-state differential pressure curves for all runs completed. All the plots show a fairly constant pressure differential with a higher pressure at the beginning of the run, then dropping slightly over the length of the run. The time scales of the plots also decrease with increasing Reynolds number, as expected due to higher flow rates. Starting with an average Reynolds number of 1.91x10^5 (a) has a duration of approximately 9 seconds, (b) has an average Reynolds number of 5.70x10^5 and duration of 2.2 seconds, and (c) has an average Reynolds number of $8.22x10^5$ and a duration of 1.9 seconds. The smaller change in steady-state duration from (b) to (c) compared to (a) to (b) is due to the volumetric flow rate depending on the square root of the pressure differential. So for higher and higher-pressure differentials there is a decreasingly smaller increase in flow rate, and therefore a smaller decrease in run duration.

4.1.1 Cavitation Detection via High Speed Camera

As mentioned in Section 2, one of the secondary goals of this experiment was to detect the presence of cavitation within the test geometry. Two complications of the acrylic test geometry and set-up were cited, now the impact of those issues will be discussed in regard to the images captured from the high-speed camera.

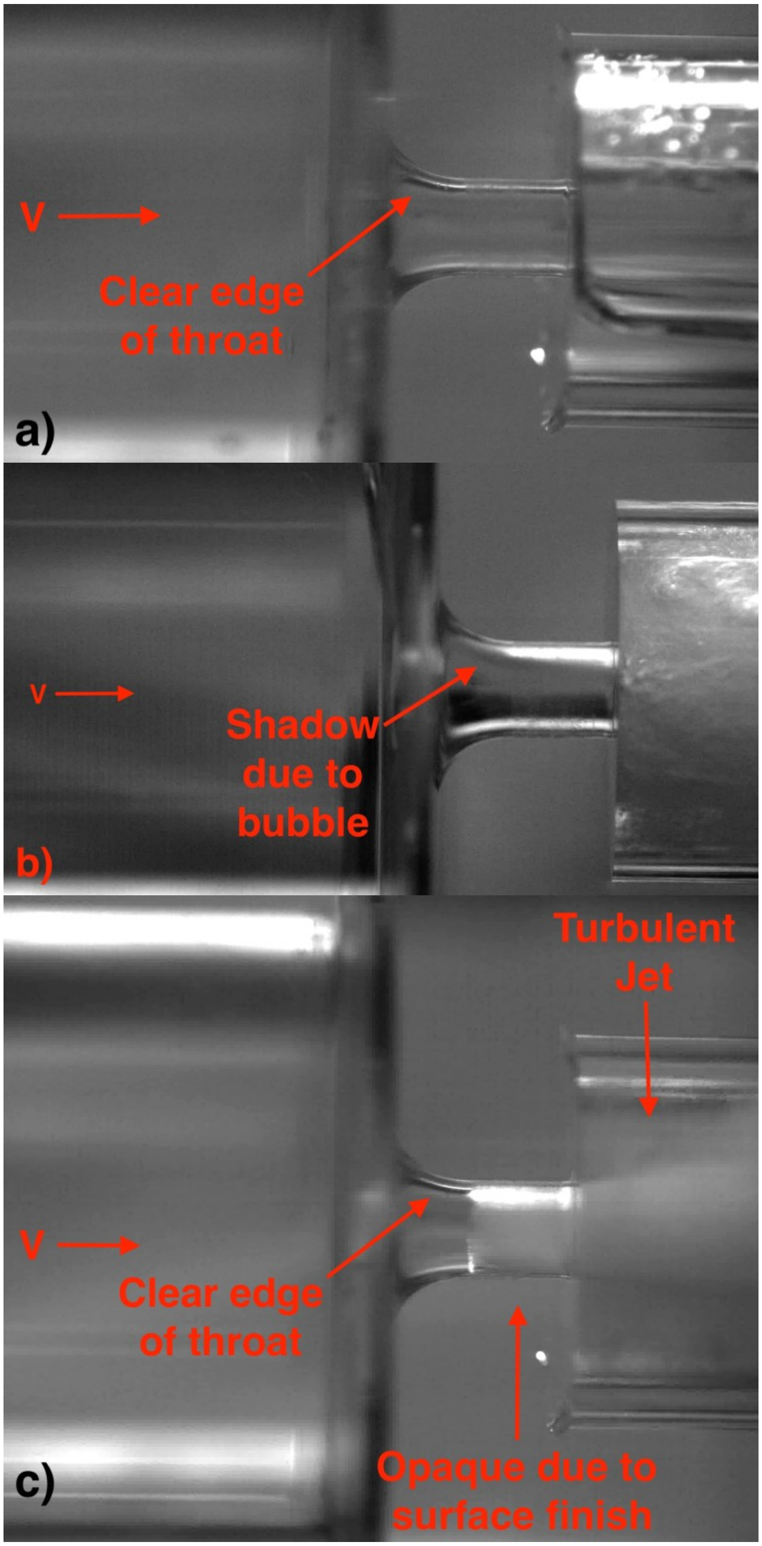

Figure 4-6: Comparison of a) fully-flooded test geometry with no flow, b) test geometry with air in throat, c) test geometry during steady-state flow rate with turbulent jet.

Figure 4-6 shows three different images of the test geometry, (a) shows the fully flooded test and highlights the lighting reflections within the converging portion of the throat. The camera was focused on the throat specifically to capture possible cavitation bubbles. This also meant these reflections were in focus, possibly obscuring cavitation bubbles. Figure 4-6a also shows the point where the surface finish of the throat no longer becomes perfectly optically clear. This can be seen by the blurring of the light reflections after the converging section of the throat. After this point in the throat, the images could not provide further evidence about the presence or lack of cavitation bubbles in the test geometry.

Figure 4-6b, shows a sample image of the test geometry during the ending phase of an experimental run. The key feature highlighted is the opaque upper region of the throat, which is in shadow due to a trapped air bubble entering the test geometry. In this sample image the cause of the opaque region in the throat is due to the bubble (and not cavitation), it serves as an example of what cavitation in the throat is expected to look like.

Lastly, Figure 4-6c shows the test geometry during the steady-state region of a high-pressure sample run. Focusing on the throat section of the geometry there is no obvious presence of an opaque "film" of air or water vapor in the converging portion. This result during steady state was consistent for all experimental runs. The opaque region in the parallel portion of the throat is due to the discontinuity in the surface because it is not optically clear. This cause of opacity is further supported by the clean break in clarity from the converging section of the throat to the parallel section.

4.1.2 Discharge Coefficient Characterization

In this subsection the average discharge coefficient for the experimental runs will be examined to characterize the test geometry's performance over the range of Reynolds numbers and cavitation numbers tested.

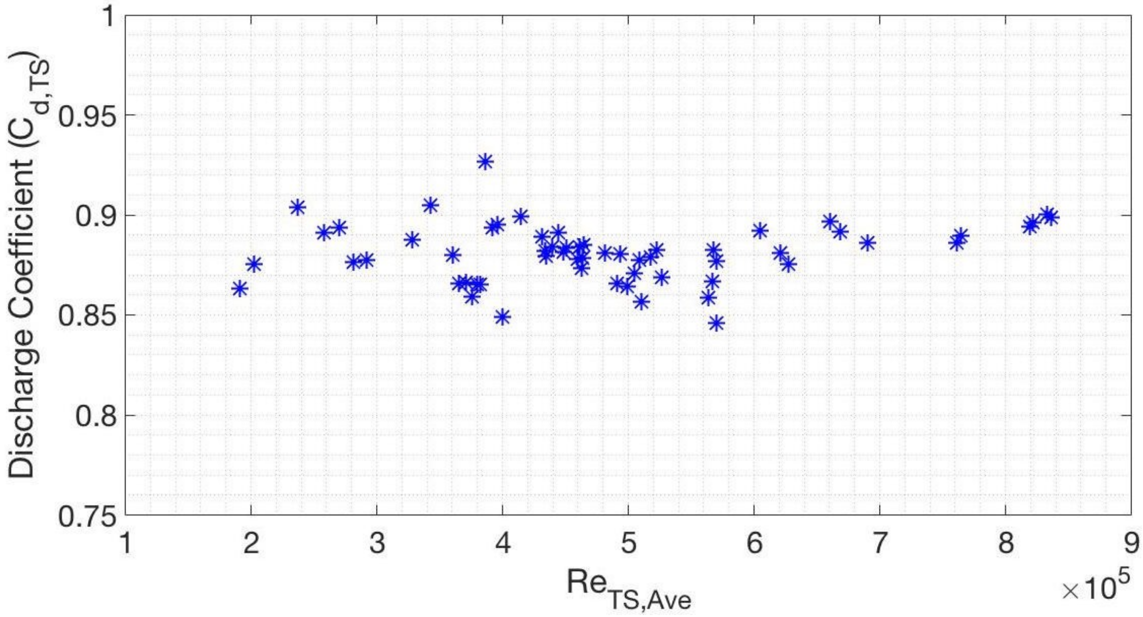

Figure 4-7: All test section discharge coefficients $C_{d,TS}$ versus average Reynolds number during steady-state flow rate.

Figure 4-7 shows the average discharge coefficient against the average Reynolds number for each experimental run during steady-state conditions. The overall shape of the results is flat, with increasing Reynolds numbers, ~1.9×10^5<Re<~8.4×10^5. Additionally, the results center on an average of 0.88 with a maximum and minimum discharge coefficient of 0.93 and 0.84 respectively, ending with a value of 0.9 at the highest Reynolds number.

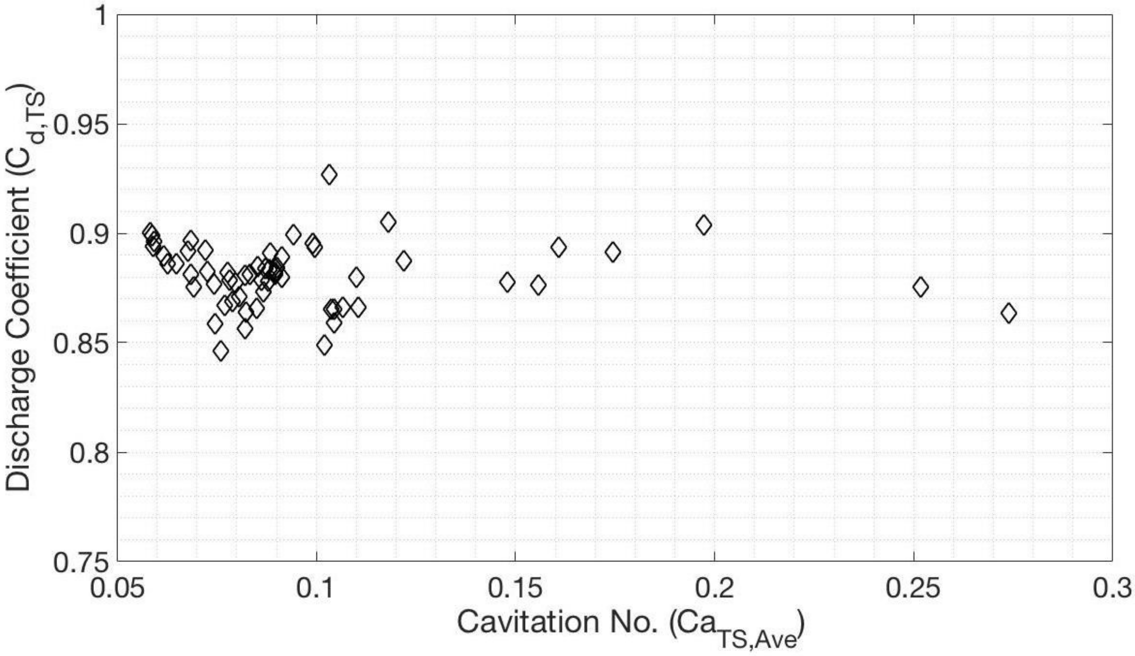

Figure 4-8: All test section discharge coefficients $C_{d,TS}$ versus average cavitation number during steady-state flow rate.

Figure 4-8, plots the same discharge coefficients; however, they are now plotted against their respective average cavitation numbers. The vast majority of the runs had cavitation number below 0.1, where it is expected for the flow to be heavily cavitating by this point. Additionally, the overall shape of the discharge coefficients remains flat over the entire range. The interpretation of these results, along with the high-speed video images will be detailed in the following subsection.

4.2 Discussion of Test Geometry Performance

After the review of the data, an in depth interpretation is required to provide a full understanding of the phenomena occurring within the test geometry. To provide this information, the high-speed images and discharge coefficients (compared to both Reynolds and cavitation number) will be examined further, as well as compared to previous research. Initially, cavitation detection and effects will be discussed before examining the results as they relate to Reynolds number.

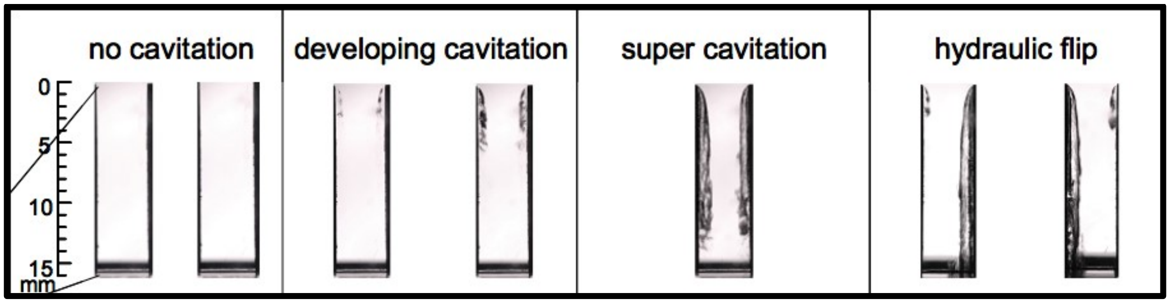

Figure 4-9: Progression of cavitation from left to right, starting with no cavitation until reaching hydraulic flip in a 2-D nozzle (Sou et al. 2007).

Figure 4-9 is recreated from Sou (2007) and shows the progression of cavitation from left to right, starting with no cavitation through its growth until it reaches the nozzle outlet, and hydraulic flip occurs. As cavitation forms and develops there is a clear vapor liquid interface along the nozzle surface.

Figure 4-6c focuses on the test geometry throat for the third highest Reynolds number ($8.22x10^5$) run performed, and lowest cavitation numbers (0.06) during steady-state conditions. This figure shows that the inlet of the throat, which is the expected location for cavitation to appear (Ebrahimi et al. 2017 and Sou et al. 2007), shows no signs of a vapor/liquid interface. From Figure 4-6b and Figure 4-9 it is expected for this region to become either opaque or a clear liquid-vapor interface to appear as in Sou et al. (2007). This implies that the rounding at the inlet of the throat delays the onset of cavitation as suggested by Spikes and Pennington (1959).

Additionally by examining Figure 4-8 from the previous subsection, the discharge coefficient of the test geometry varies very little with cavitation number. For this to be the case, two different scenarios could be occurring during the experimental runs:

1. Cavitation does not occur and the flow remains single-phase for all runs completed.
2. Cavitation bubbles do not form within the test geometry, but actually occur downstream.

Due to such a low cavitation number for this run, Ca = 0.06, along with all the runs for this experiment, it is unlikely that cavitation is not occurring in the test geometry; consequently, it is unlikely the first scenario is realistic.

Based on the assumptions and conclusions drawn from Ramamurthi and Nandakumar (1999) and Spike and Pennington (1959) it is likely that the flow actually cavitates downstream of the test geometry, never affecting the discharge coefficient. As a reminder, they concluded that a cavitation bubble would collapse at a length of L/D = 5 downstream of the orifice inlet for viscous flows, and that smaller L/D ratios move the cavitation zone of the flow downstream of the orifice, respectively. This scenario is further supported by Brennen (2005). He presented that in low-pressure flows, such as the one found in the test geometry throat, microscopic cavitation bubbles could form, but could pass through without issue if there was not sufficient time for the bubble to grow in size.

Now focusing on the discharge coefficient in relation to Reynolds number, a few conclusions can be drawn when compared to previous research. First, there is no significant decrease or drop off of the discharge coefficient for the range of Reynolds numbers tested. Based on Chemloul (2011) and Ramamurthi and Nandakumar (1999), once cavitation inception occurs within the test geometry, there is a sudden drop off in orifice performance. As a reminder, their findings are shown in Figure 1-5 in Section 1.5. This lack of drop-off also suggests that either no cavitation occurs for any run or that cavitation is present for all runs but has no effect on discharge coefficient. Again, the latter scenario is more likely given the range of cavitation numbers presented in this thesis.

In fact, the discharge coefficient remained relatively constant over the range of Reynolds numbers tested, varying only +5% above or -4% below the average value of 0.88. This trend is shown in Figure 4-10 below.

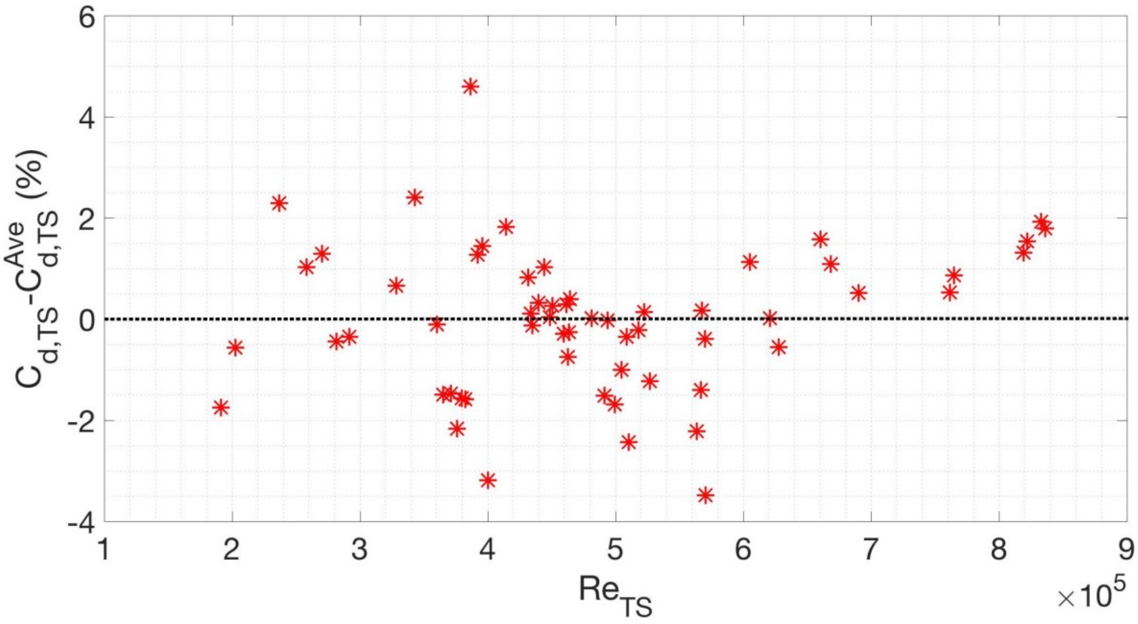

Figure 4-10: Percent variation in discharge coefficient from average value for all experimental runs.

This independence of discharge coefficient with respect to Reynolds numbers above 10^5 has been shown in previous single-phase research including Lichtarowicz et al. (1965) and Hall (1963). A summary plot of Hall's theoretical equation along with other experimental data is shown below.

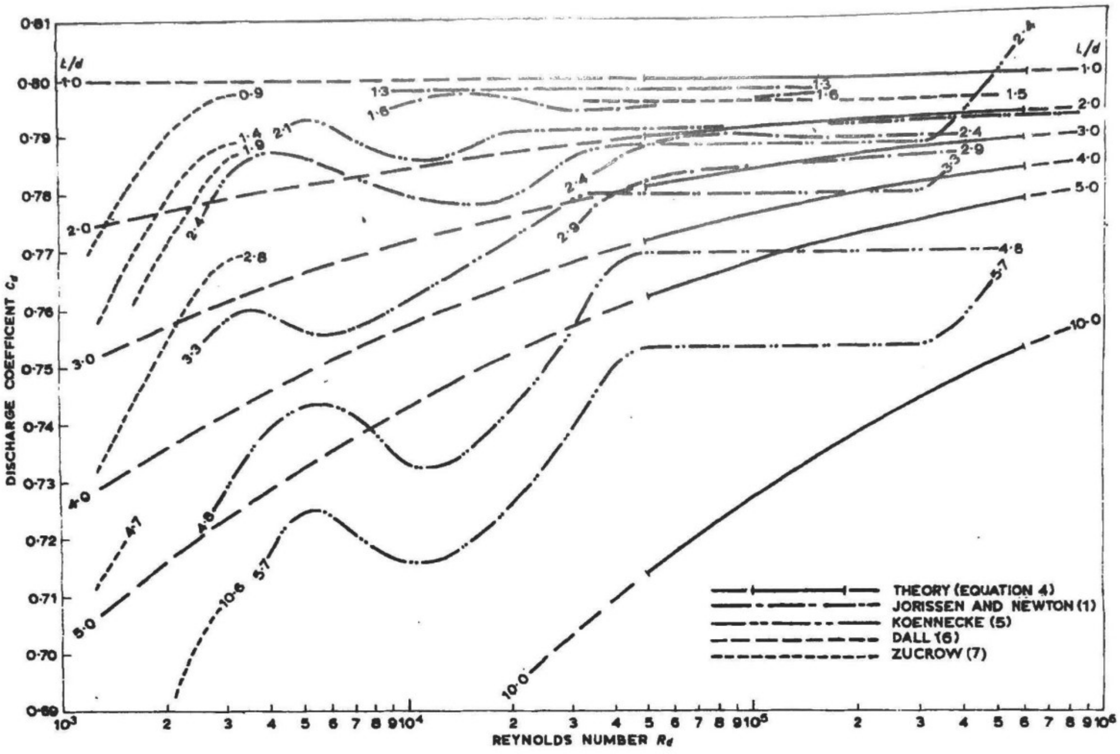

Figure 4-11: Discharge coefficients for a range different L/D values for cylindrical-tube orifices summarized by Hall (1963).

For all data with an L/D≈2, the discharge coefficient becomes independent of Reynolds number once it reaches 2×10^5. Also, the ranges of discharge coefficient maximum are of particular interest, starting at 0.76 and increasing to 0.8 with increasing Reynolds number. Lichtarowicz et al.

(1965) also showed that this was the maximum discharge coefficient. This asymptotic maximum value is of particular interest as it is 9% or 5.5 standard deviations (based on data from this thesis) below the average discharge coefficient for the test geometry.

This increase in discharge coefficient maximum is suspected to be caused by the rounded inlet of this thesis' test geometry and this assertion is supported by the results from Hobbs and Humphreys (1990) and Kent and Brown (1983). For Kent and Brown (1983) there was as much as an ~19%[†] increase in discharge coefficient by increasing the inlet rounding from r/d = 0 to r/d =1. For this thesis, r/d = 0.75, which correlated to a 9% increase from sharp-edged discharge coefficients based on Hall (1963). Characterizing the exact effect inlet rounding had on discharge coefficient was outside the scope of this thesis, but this correlation does provide an interesting point of comparison.

4.3 Test Facility Performance and Discussion

The test facility was built specifically for this thesis. As such, its overall performance will be briefly addressed. First, by revisiting the requirements for the facility's construction, and determining if those

---

[†] Empirically determined from plots

requirements were achieved; then by examining and interpreting the data collected.

First, the test facility was only able to supply a pressure differential of 1200 psid across the test section, opposed to required 2500 psid. However, the test geometry discharge coefficient became independent of Reynolds number under tested conditions so reaching the maximum pressure was no longer required. Next, the test facility was sufficiently instrumented to allow researchers to investigate phenomena occurring within the test geometry, including characterization of the discharge coefficient. Additionally, the facility was properly designed to allow for high-speed video of the test geometry during steady-state conditions. Finally, there was no corrosion in the test facility due using water as the working fluid, and as a result did not have any observable effects on the data. Overall the design requirements for the test facility were met, although the maximum pressure differential was not reached, sufficient data was collected to show that discharge coefficient had become independent of Reynolds number.

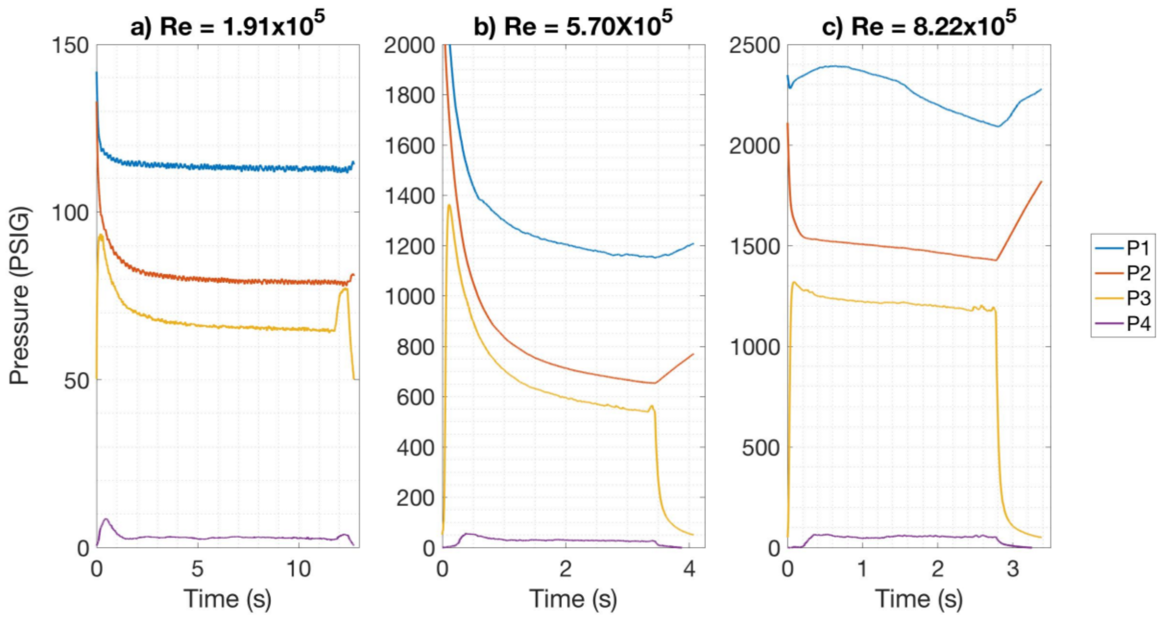

Figure 4-12: Measured pressures throughout test facility for three different experimental runs at varying regulator outlet pressures (P1).

Figure 4-12 shows pressures recorded throughout the test facility for different experimental runs over the full range of Reynolds numbers tested. As a reminder, pressure sensors P1 (outlet of regulator) and P2 (upstream of high-pressure cylinder) are upstream of the firing valve, which is why they measure high pressures before and after the steady-state region of the runs. Pressure sensors P3 and P4 are directly upstream and downstream of the test section.

For all Reynolds numbers (a-c) the pressure drop from P1 to P2, through the nitrogen subsystem, was roughly the same order of magnitude as the pressure drop across P3 and P4, the test section. This pressure drop in the nitrogen subsystem was an issue as it lowered the upper limit of Reynolds numbers that could be tested with the facility. As mentioned in Section 2, modifications were made to decrease the pressure drop through the nitrogen system. These plots include experimental runs after those modifications, and represent the test facilities with the smallest pressure loss.

It can be shown from plots a-c, that the pressure drop between sensors P1 and P2 increases with increasing output pressure from P1 during the steady-state phase of each run. This trend is evidence that the entire test facility follows steady-state incompressible behavior, which is governed by Bernoulli's equation with head loss. This fact was further proven in Appendix B when the maximum velocity of the nitrogen gas for all experimental runs was calculated and was 0.25 Mach. For gas flows with a velocity below 0.3 Mach it can be assumed the flow is essentially incompressible (Kundu et al. 2012) (Pritchard 2011). The generalized equation for head loss, which was shown in the Introduction, has been modified below to show the dependence head loss has on the measured pressure differential between two points.

$$H_L = fC_d^2 \frac{L}{D} \frac{\Delta p}{1 - \beta^4} \tag{4-1}$$

This equation shows there should be a linear correlation between pressure differential and head loss, which the test facility exhibits. To further demonstrate this, in Figure 4-13 (shown below) the pressure differential between P1 and P2, as well as the differential between P2 and P3 are plotted as a function of P1. The three different groupings of linear lines correlate to updates made to the nitrogen subsystem to eliminate head loss. Within each grouping, it is clear that there is a linear trend through the data.

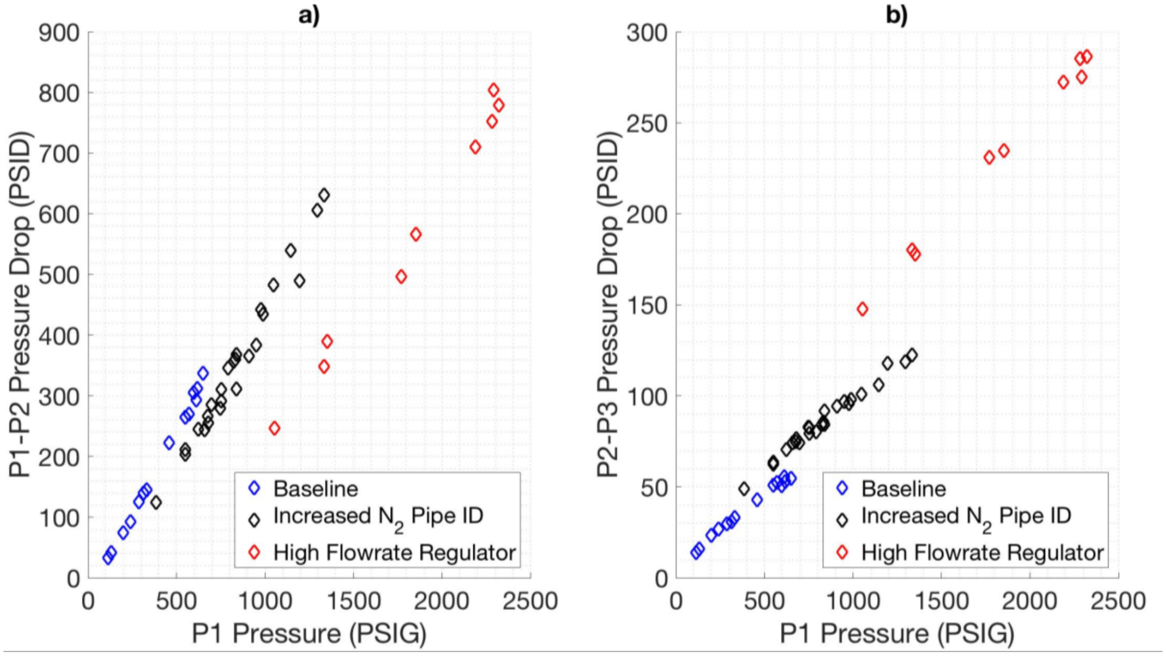

Figure 4-13: a) Pressure drop through nitrogen subsystem for all experimental runs, b) Pressure drop through water subsystem for all experimental runs.

Additionally, comparing the two plots also shows an interesting correlation. For runs with a higher pressure-drop rate between P1 and P2, there is a decreased pressure-drop slope between P2 and P3, and vice versa. This phenomenon can be attributed to the pressure drop between two points in the system is due to a combination of both head loss and the conversion of static pressure to dynamic pressure.

The cause for the inversing of slopes between the two subsystems for the same modifications is: head loss is the major contributing factor to the change in pressure drop in the nitrogen subsystem, so as the updates are made, the slope decreases. Whereas the increase in pressure drop in the water subsystem is due to the increased flow rate, which corresponds to increased dynamic pressure and head loss. Finally, this comparison shows that to further increase the range of Reynolds numbers that the facility can test, the majority of the head loss should be isolated to the water subsystem (between P2 and P3) as the pressure drop rate was significantly higher in the nitrogen subsystem (between P1 and P2).

5 Test Facility Recommendations

Over the course of the experiment, unpredicted issues arose which were not expected during the initial design and assembly of the facility. Additionally, these issues were either fixed during testing or accounted for during the analysis. This section highlights these issues and suggests recommendations if future research is conducted using this test facility.

The recommendations are broken down into two categories; all physical updates related to the design of the test facility, and data collection updates to provide further insight into the phenomena occurring in the test geometry.

5.1 Physical Design Recommendations

The first major issue arose during the assembly and pressure testing of the experimental facility. The pipes selected for the water subsystem were threaded, which meant the orientation of the fittings was effected by the ability to fully seal the pipes. This situation led to the possibility of over or under tightening connections to properly align pipes during assembly. Additionally, the pipe sealant selected did not provide a sufficient seal at higher pressures, approximately 2000 psig and above, even though it was rated for 10,000 psig. This meant over the course of the experiment, small droplets of water formed at pipe connections; subsequently the test facility was broken down, cleaned, and reassembled to create better seals.

To fix this in future testing, it is recommended that flanged pipe connections sealed via O-rings, be used on the water subsystem. This approached allows for the alignment of pipe and sealing of the fittings to be independent of one another as well as provides a better seal. The test section, which was sealed using O-rings, never exhibited any leaking over the course of experimentation. The nitrogen system used Yor-Lock fittings, which allow for proper sealing of pipes and fittings for any orientation, and sealed sufficiently over the course of experimentation as well.

Also, any steps to decrease head loss throughout the test facility should be explored. There was major pressure drop between P1 and P2, which decreased the maximum pressure differential across the test section, ΔP34. By decreasing these drops, a larger range of pressure differentials could have been tested for the test geometry, providing a larger range to characterize the discharge coefficient. Equation 2-1 shows the major components for head loss for a given volumetric flow rate.

It is clear the dominating factor is pipe diameter. By simply increasing pipe diameters for a given flow rate, head loss would drop significantly. This recommendation was done for the nitrogen subsystem by increasing pipe diameters from ¼" to $^3/_8$", however other changes such as decreasing the number of fittings and pipe lengths could not be changed do to the limitations of the laboratory layout and space.

Next, for future testing, the parallel section of the test geometry needs to be re-polished until it is optically clear. For the experiments covered in this thesis, it could not be directly determined from the high-speed images if cavitation bubbles were present in this section of the throat. This was partly due to surface finish of the acrylic. While the pressure data and previous research suggests they were not, clear images of the throat would provide further evidence to support this conclusion.

The final recommendation is to ensure the water subsystem could be fully flooded, which would prevent any local variation in flow due to air bubbles trapped in the system. To do this, the firing valve would be moved downstream of the test section, as well as creating a high point with a bleed valve in the water subsystem. These two changes would allow for the test section to be flooded during the entirety of each experimental run as well as remove essentially all trapped air in the water subsystem prior to testing.

5.2 Data Recommendations

The first recommendation would be the removal of the ultrasonic flow rate sensor, while adding a standard pitot tube to measure flow rate.

Initially, the goal was to prevent any perturbation to the flow prior to entering the test section; however, this resulted in using a flow rate sensor, which lagged during such short-term steady-flow conditions. The pitot tube, which would cause little disturbance to the flow due its low profile, could be placed significantly upstream of the test section. As stated in Section 2, the flow rate sensor needed a significantly long section of pipe prior to and after it to provide accurate measurements, this same section would provide enough distance for any disturbances from the pitot tube to dissipate, while providing instantaneous flow measurements.

Next, an additional pressure sensor would be added just after the high-pressure cylinder in the water subsystem. This would allow for a more accurate measurement of the pressure drops across the water subsystem and high-pressure cylinder. These measurements could be used as a check to ensure the flow rate measured (by the pitot tube) was accurate. It would also provide more data to pinpoint higher pressure-loss areas in the test facility, which could subsequently be removed.

Finally, the last recommendation would be to increase the frame rate of the high-speed camera. During experimentation, while the frame rate was varied, it was never set high enough to capture completely still images of the flow through the throat of the test geometry. This was due to estimating the frame rate needed to capture still images of the flow prior to entering the throat. The increased frame rate would allow for the possible visual detection of cavitation bubbles forming during a run, which is expected based on the cavitation number range presented in this thesis.

6 Conclusion

A test facility was designed and built to characterize the discharge coefficient for a specific round-edged orifice plate geometry, along with a secondary goal of determining the presence of different flow phenomena over the range of pressure differentials tested. The results showed that for the range of Reynolds numbers in this thesis the test geometry exhibited similar discharge coefficient behavior to other orifice geometries; specifically, the coefficient became independent of Reynolds number for values above 10^5. The results also showed that the asymptotic value of the test geometry discharge coefficient was above that of sharp edged orifice plates but below those of other orifice designs.

Additionally, the results showed that the discharge coefficient was insensitive to changes in cavitation number. This result was further corroborated by high-speed video data, which showed no clear presence of cavitation or hydraulic flip inside the test geometry throat for any experimental run. It has been noted the high-speed video may have not been able to detect the presence of cavitation bubbles in the throat due to lower frame rates and parts of the throat not being optically clear.

The test facility built for this experiment met the majority of the preliminary requirements, with the exception of reaching a maximum differential pressure of 2500 psid across the test geometry. It was later determined that this requirement was not needed as the asymptotic value of the discharge coefficient was reached. Over the course of the experiment updates to the test facility were made to further increase the maximum pressure differential across the test geometry. Finally, recommendations were made to increase the pressure operating range of the test facility and to further investigate the test geometry to characterize the discharge coefficient and associated phenomena.

Appendix A Test Geometry Technical Drawings

This appendix contains all the technical drawings of the test section. They are shown in the following order: Test Section Assembly, Acrylic Test Block, Inlet Flange, Outlet Flange and Flange Adapter.

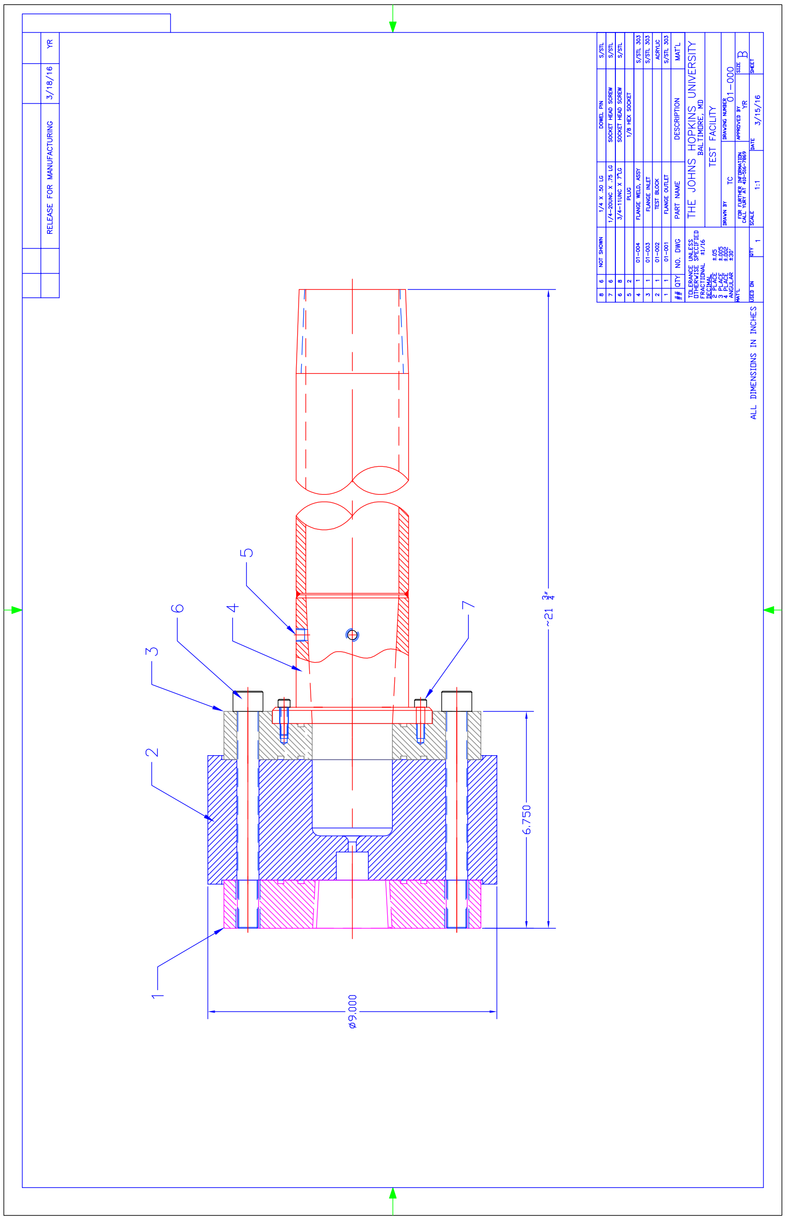

##	QTY	NO. DWG	PART NAME	DESCRIPTION	MAT'L
8	6	NOT SHOWN	1/4 X .50 LG	DOWEL PIN	S/STL
7	6		1/4-20UNC X .75 LG	SOCKET HEAD SCREW	S/STL
6	8		3/4-11UNC X 7"LG	SOCKET HEAD SCREW	S/STL
5	2		PLUG	1/8 HEX SOCKET	
4	1	01-004	FLANGE WELD, ASSY		S/STL 303
3	1	01-003	FLANGE INLET		S/STL 303
2	1	01-002	TEST BLOCK		ACRYLIC
1	1	01-001	FLANGE OUTLET		S/STL 303

Figure A-1: Technical drawing of test section assembly.

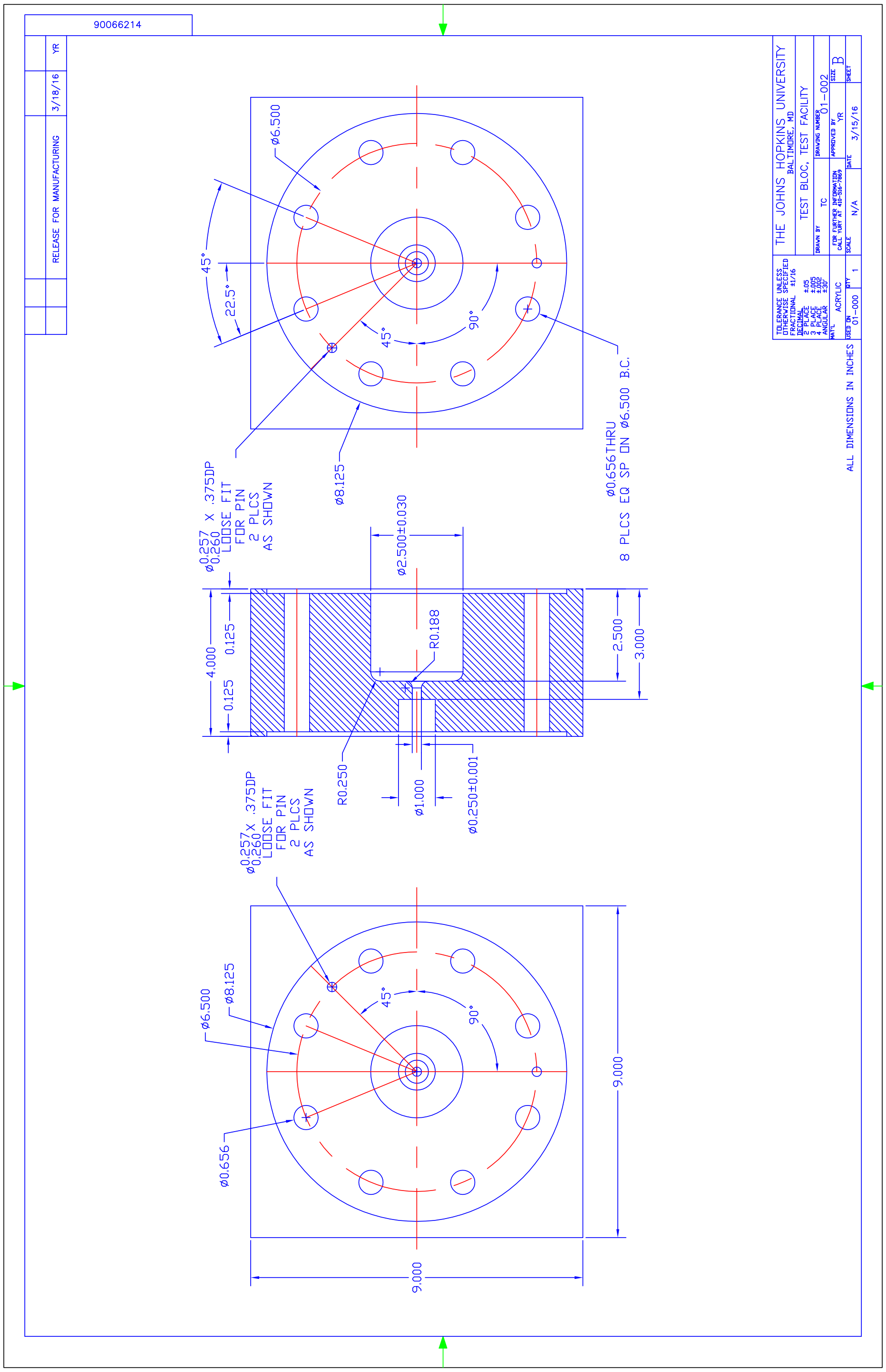

Figure A-2: Technical drawing of test block.

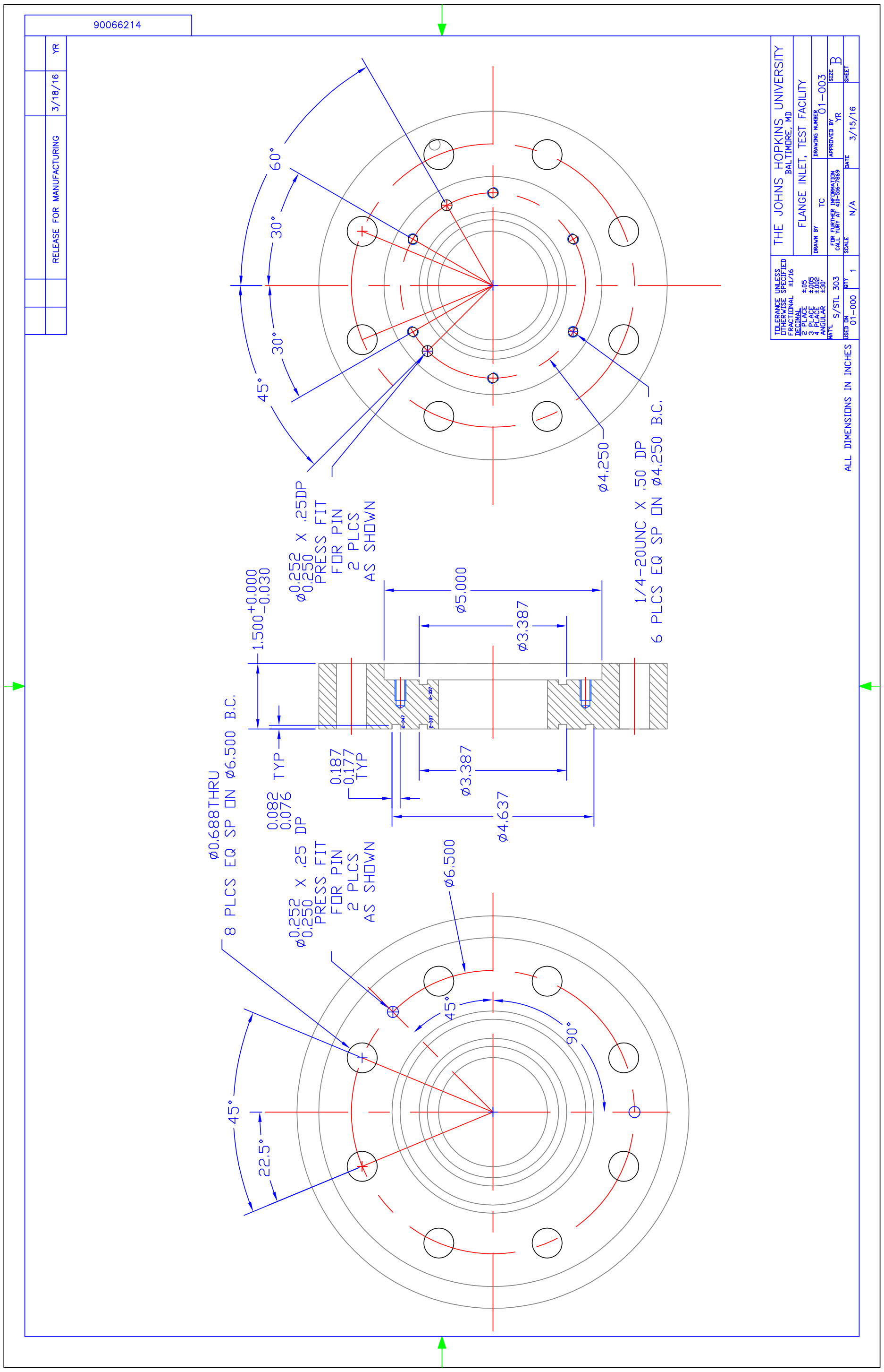

Figure A-3: Technical drawing of inlet flange.

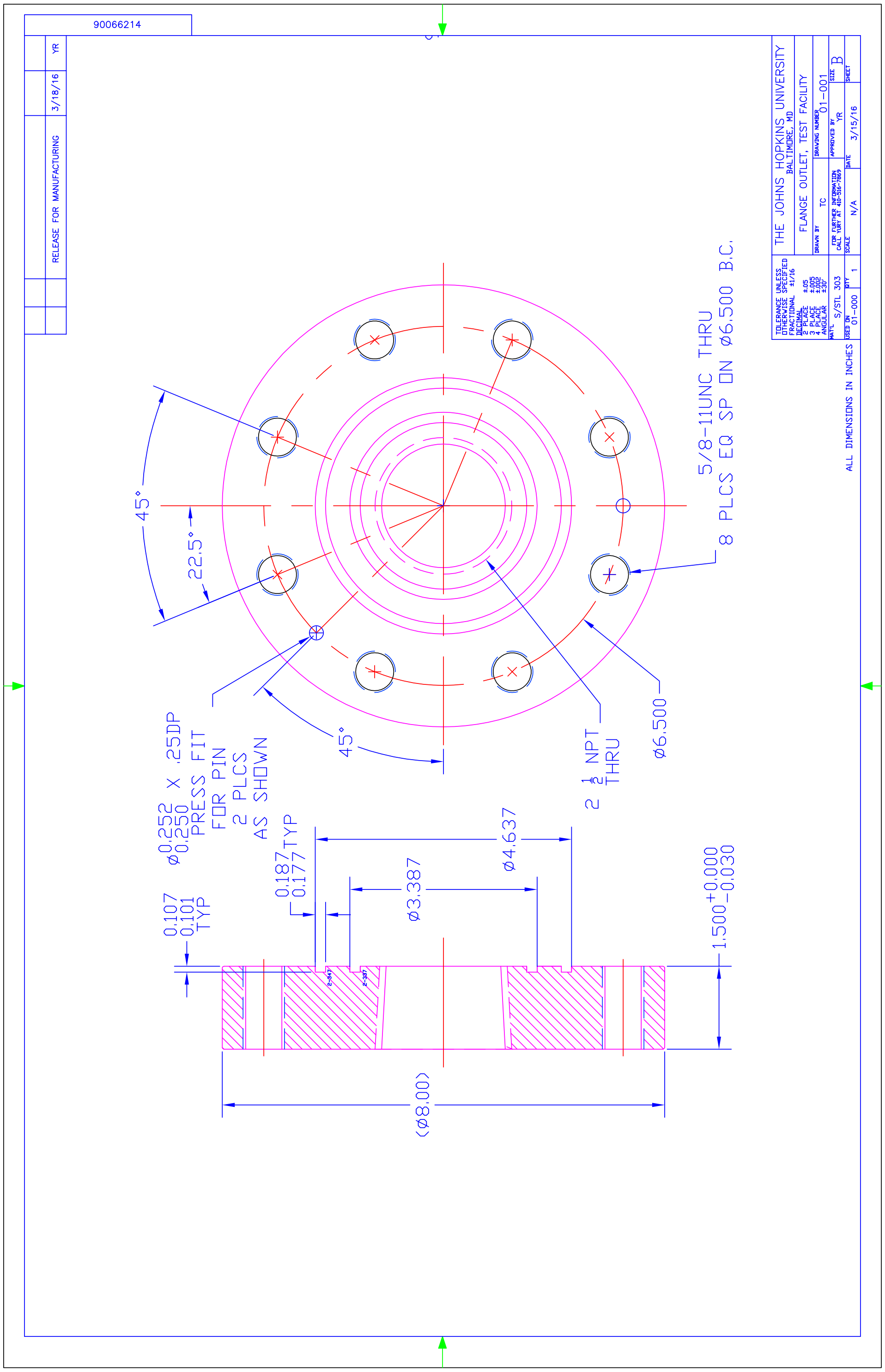

Figure A-4: Technical drawing of outlet flange.

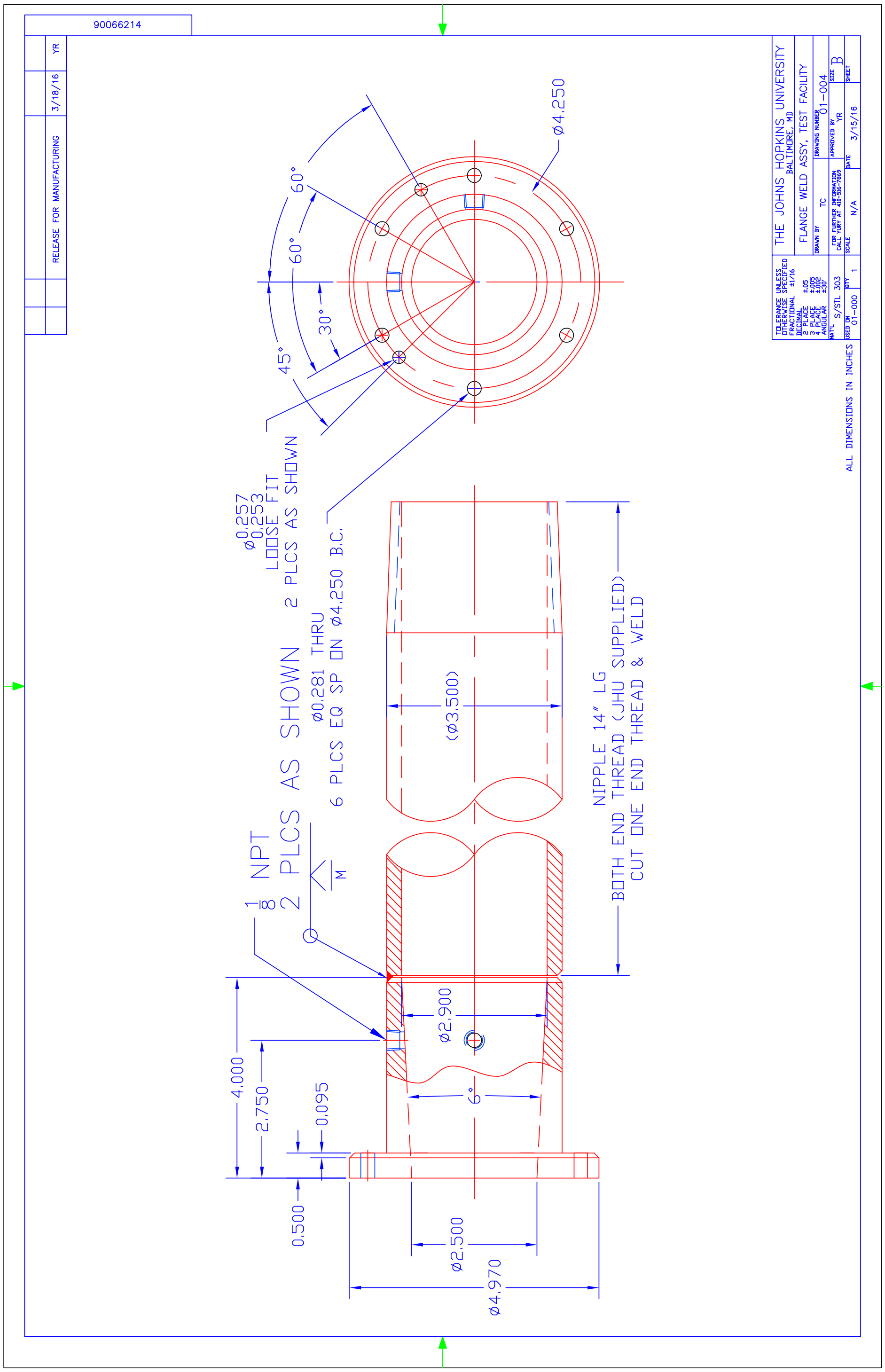

Figure A-5: Technical drawing of flange pipe adapter.

Appendix B Head Loss Calculations

This appendix outlines the assumptions and equations used to determine the head loss between pressure transducer P2 and the pressure inside the cylinder, PC, as well as P3 and the pressure just after the cylinder, PAC. These calculations were used to determine the average discharge coefficient for the high-pressure cylinder, $C_{d,Cyl,}$ as well as, the average discharge coefficient for the water subsystem, $C_{d,H20}$. These calculations were only done for the eight low-pressure tests used to determine $C_{d,H20}$.

Nitrogen Gas Compressibility

Before the head loss can be calculated between P2 and PC, it must be determined if Bernoulli's equation is applicable to the nitrogen subsystem, and to do this the maximum velocity of the nitrogen gas during the steady-state portion of the experimental run with the highest flow rate (for all tests completed) must be checked.

Assumptions: Volumetric flow rate of entire test facility during steady state is constant.

$$\dot{V}_{34} = \dot{V}_2$$

Then using the maximum volumetric flow rate, the maximum velocity and Mach number could be calculated at P2, which has the smallest diameter in the system.

$$\dot{V}_{2,Cyl}^{max} = \nu_2^{max} A_2$$

$$\nu_2^{max} = \dot{V}_{2,Cyl}^{max} \frac{4}{\pi D_2^2}$$

Now substituting in known values, which are shown below, velocity and Mach number at P2 can be determined.

$$\dot{V}_{2,Cyl}^{max} = 252.66\ in^3/s$$

$$D_2 = 0.302\ in$$

$$c = 13872\ in/s$$

$$\nu_2^{max} = 3547\ in/s$$

$$M_2^{max} = 0.25\ \therefore\ incompressible\ flow$$

Because the flow is shown to be incompressible, Bernoulli's equation for steady-state, incompressible, viscous flow can be used to determine the pressure drop from P2 to PC. To determine the gas density, pressure measurements at P2 and the ideal gas law were used.

$$p = \rho R_{N2} T$$

Using this equation to solve for the density of the nitrogen gas for the eight low-pressure experimental runs resulted in the following range of densities:

$$11 < \rho_{N2} < 28\ kg/m^3$$

Note that these densities are two orders of magnitude below the normally assumed density of water, 1000 kg/m^3. Moving on to Bernoulli's equation:

$$p_2 + \frac{\rho_{N2}}{2}\nu_2^2 = p_C + \frac{\rho_{N2}}{2}\nu_C^2 + H_L$$

Where the equation for head loss due to the expansion into the cylinder is:

$$H_L = \rho_{N2}\frac{\nu_2^2}{2}$$

Then substituting this back into Bernoulli's equation and solving for PC:

$$p_C = p_2 + \frac{\rho_{N2}}{2}(\nu_2^2 - \nu_C^2) + \rho_{N2}\frac{\nu_2^2}{2}$$

$$p_C = p_2 + \frac{\cancelto{0}{\rho_{N2}}}{2}(\nu_2^2 - \nu_C^2) + \cancelto{0}{\rho_{N2}}(\frac{\nu_2^2}{2})$$

$$\therefore p_C = p_2$$

Due to the densities for these experimental runs being so low there was essentially no pressure loss due to expansion.

Pressure Downstream of High-Pressure Cylinder (PAC)

Again, Bernoulli's equation for steady-state, incompressible, viscous flow will be used to determine the pressure just after the high-pressure cylinder (PAC). Since the working fluid is water, it is assumed the flow is incompressible and the Bernoulli's equation is:

$$(p_{AC} + \frac{\rho_{H20}}{2}\nu_{AC}^2) - (p_3 + \frac{\rho_{H20}}{2}\nu_3^2) = \sum H_L$$

Which can be rearranged to solve for PAC:

$$p_{AC} = p_3 + \frac{\rho_{H20}}{2}(\nu_3^2 - \nu_{AC}^2) + \sum H_L$$

The total head loss in the system, ΣH_L, is due to a combination of fittings, expansions (ΔArea), pipes, and hoses.

$$\sum H_L = \sum H_{L,pipe} + \sum H_{L,fittings} + \sum H_{L,\Delta Area} + H_{L,Hose}$$

For this test facility, this included: 2x3" couples, 3"x36" long pipe, 2" to 3" expansion, 2" ball valve, 1" to 2" expansion, 1" through tee, 2x1" branch tee, 1" elbow, 1"x5' long hose, and ½" to 1" expansion. The general equations for each group are:

$$H_{L,pipe} = f_D \rho_{H20} \frac{L}{D} \frac{\nu_D^2}{2}$$

$$H_{L,fittings} = f_D \rho_{H20} \frac{L_{equivalent}}{D} \frac{\nu_D^2}{2}$$

$$H_{L,\Delta Area} = K_{equivalent} \frac{\nu^2}{2}$$

$$H_{L,Hose} = 0.0018(FR_{GPM})^{1.77}$$

Where $L_{equivalent}$, and $K_{equivalent}$ was provided by Pritchard (2011). As mentioned in Section 3, Blasius' approximation was used to determine the friction factor. Below are the calculations used to determine if the approximation was reasonable for the range of Reynolds numbers for the eight experimental runs. As a reminder, the approximation is shown below along with the Reynolds number range.

$$f_{D,Blasius} = \frac{0.0791}{Re_D^{0.25}}$$

$$4000 \leq Re_D \leq 10^5$$

Then calculating the ideal Reynolds number for the maximum case, which would be the smallest diameter pipe at the highest flow rate, and the minimum case, or the largest diameter pipe at the lowest flow rate, the results are:

$$Re_{Max,D=1"} = 2.2 \times 10^5$$

$$Re_{Min,D=3"} = 1.4 \times 10^4$$

While the maximum Reynolds number is slightly high, these were ideal values, and therefore the actual maximum would be lower, so it was assumed this was acceptable.

Appendix C Results Summary

Test Section ΔP34 (psid)	Average Reynolds Number, Re_{Ave}	Average Cavitation Number, Ca_{Ave}	Test Section Discharge Coefficient, $C_{d,TS}$
62.93	1.91E+05	0.27	0.86
70.62	2.03E+05	0.25	0.88
96.43	2.37E+05	0.20	0.90
114.58	2.58E+05	0.17	0.89
125.47	2.70E+05	0.16	0.89
136.30	2.82E+05	0.16	0.88
146.18	2.92E+05	0.15	0.88
184.98	3.28E+05	0.12	0.89
202.17	3.43E+05	0.12	0.90
222.94	3.60E+05	0.11	0.88
229.09	3.65E+05	0.11	0.87
236.75	3.71E+05	0.11	0.87
242.88	3.76E+05	0.10	0.86
247.62	3.80E+05	0.10	0.87
250.96	3.82E+05	0.10	0.87
256.44	3.86E+05	0.10	0.93
264.26	3.92E+05	0.10	0.89
269.12	3.96E+05	0.10	0.90
275.15	4.00E+05	0.10	0.85
295.00	4.14E+05	0.09	0.90
319.95	4.32E+05	0.09	0.89

323.04	4.34E+05	0.09	0.88
324.92	4.35E+05	0.09	0.88
331.72	4.40E+05	0.09	0.88
338.96	4.44E+05	0.09	0.89
345.79	4.49E+05	0.09	0.88
348.56	4.51E+05	0.09	0.88
362.80	4.60E+05	0.09	0.88
365.72	4.62E+05	0.09	0.88
367.60	4.63E+05	0.09	0.87
369.20	4.64E+05	0.09	0.88
370.33	4.64E+05	0.09	0.88
397.42	4.81E+05	0.08	0.88
414.20	4.91E+05	0.08	0.87
418.36	4.94E+05	0.08	0.88
427.99	4.99E+05	0.08	0.86
437.20	5.05E+05	0.08	0.87
444.00	5.09E+05	0.08	0.88
446.96	5.10E+05	0.08	0.86
460.59	5.18E+05	0.08	0.88
468.86	5.23E+05	0.08	0.88
476.25	5.27E+05	0.08	0.87
544.97	5.63E+05	0.07	0.86
551.53	5.67E+05	0.08	0.87
553.45	5.68E+05	0.07	0.88
557.65	5.70E+05	0.07	0.88
558.54	5.70E+05	0.08	0.85
628.22	6.05E+05	0.07	0.89
661.47	6.21E+05	0.07	0.88

676.42	6.28E+05	0.07	0.88
748.61	6.60E+05	0.07	0.90
766.88	6.68E+05	0.07	0.89
817.55	6.90E+05	0.06	0.89
995.81	7.62E+05	0.06	0.89
1003.68	7.65E+05	0.06	0.89
1152.48	8.19E+05	0.06	0.89
1159.82	8.22E+05	0.06	0.90
1191.52	8.33E+05	0.06	0.90
1200.23	8.36E+05	0.06	0.90

Table 3: Summary of Experimental Results

References

Ashrafizadeh, S.M. and Ghassemi, H. 2015. “Experimental and numerical investigation on the performance of small-sized cavitating venturis”. *Flow Measurement and Instrumentation*. 42. 6-15

ASTM. 1967.“Erosion by cavitation or impingement,” *Amer. Soc. for Testing and Materials*, ATSM STP408.

Beer, F.P., Johnston, E.R., et al. 2011. *Statics and Mechanics of Materials,* 1st ed. New York, New York:McGraw-Hill, pp. 592-594, 606-616

Billet, M. L. 1985. “Cavitation nuclei measurement-a review,” Proc. *1985 ASME Cavitation and Multiphase Flow Forum*, pp. 31-38

Blake, F.G., “The onset of cavitation in liquids,” *Acoustics Res. Lab.*, Harvard University, Tech. Memo. No. 12

Brennen, C.E. 1995. Cavitation and Bubble Dynamics, 1st ed. New York, New York: Oxford University Press.

Brennen C.E. 2005. Fundamentals of Multiphase Flows, 1st ed. New York, New York: Cambridge University Press.

Chemloul, N.S. 2012. Experimental Study of Cavitation and Hydraulic Flip Effects on Liquid Jet Characteristics into Crossflows. *Journal of Applied Fluid Mechanics*. 5. 33-43.

Desantes JM, Lopez JJ, Carreres M, and Lopez-Pintor D. 2016. “Characterization and prediction of the discharge coefficient of non-cavitating diesel injection nozzles”. *Fuel*, 184:371-381

Ebrahimi, Behrouz, He, Guoliang, Tang, Yingjie, Franchek, Matthew, Liu, Dong, Pickett, Jay, Springett, Frank, Franklin, Dan. 2017.“Characterization of high-pressure cavitating flow through a thick orifice plate in a pipe of constant cross section”. *International Journal of Thermal Sciences*.

Fujikawa, S. and Akamantsu, T. 1980. “Effects of the non-equilibrium condensation of vapour on the pressure wave produced by the collapse of a bubble in a liquid.” *J. Fluid Mech*. 97, pp. 481-512

Grey, R.E. and Wilsted, H.D. 1949. “Performance of concial jet nozzles in terms of flow and velocity coefficients”. *Nat. Advisory Committee for Aeronautics.*

Hall, G.W. 1963. “Analytical determination of the discharge characteristics of cylindrical-tube orifices”. *J Mech E Sci*, 5:1. pp.91-97.

Hebbar, Sheshagiri K and Sridhara, K and Paranjpe, PA. 1970. “Performance of conical jet nozzles in terms of discharge coefficient”*, Journal of Aeronautical Society of India*, 22:1. pp. 3-9.

Hobbs, J.M., and Humpherys, J.S. 1990. “The effect of orifice plate geometry upon discharge coefficient”. Flow Measurement Instrumentation, 1:133-140

Hose Master PressureMax HP Corrugated Hose, Hose Master LLC., Cleveland, Oh, 2017, www.hosemaster.com/technical-information/pressure-drop/.

Kent, J.C., and Brown, G.M. 1983. “Nozzle Exit Flow Characteristics for Square-edged and Rounded Inlet Geometries”. *Combustion Science and Technology*, 30:16:121-132

Kiljański, Tomasz. 1993. “Discharge Coefficient for Free Jets From Orifices at Low Reynolds Number”. *Journal of Fluids Engineering-transactions of The Asme - J FLUID ENG*. 115.

Kundu, P. K., Cohen, I. M., and Dowling, D.R. 2012. “Compressible Flow,” Fluid Mechanics, 5th ed. Oxford, UK: Academic Press, 2012, ch. 15, pp. 730-778

Lichtarowicz, A.K., Duggins, R.K., and Marland E. 1965. “Discharge coefficients for incompressible non-cavitating flow through long orifices”. *J Mech Eng Sci*, 7:210-219

Moin, P., “Numerical Differentiation - Finite Differences,” Fundamentals of Engineering Numerical Analysis, 2nd ed. New York, New York: Cambridge University Press, ch. 2, pp.13-30

Neppiras, E.A. and Noltingk, B.E., “Cavitation produced by ultrasonics: theoretical conditions for the onset of cavitation.” *Proc. Phys. Soc.*, London, 64B, pp. 1032-1038

Parker O-Ring Handbook, Y2000 ed., Parker Hannifin Corp., Lexington, KY, 2000, pp.4-2:4-16

Plesset, M.S. 1949 “The dynamics of cavitation bubbles.” *ASME J. Appl. Mech.* 16, pp. 228-231

Pritchard, P.J. 2011. “Internal Incompressible Viscous Flow,” Fox and McDonald’s Introduction to Fluid Mechanics, 8th ed. Hoboken, NJ: Wiley, ch. 8, pp. 356-396

Ramamurthi, K., and Nandakumar, K. 1999. “Characteristics of flow through small sharp-edged cylindrical orifices”. *Flow Measurement and Instrumentation*,10:133-143

Reader-Harris, M. 2015. Orifice Plates and Venturi Tubes, 1st ed. Cham, Switzerland: Springer International Publishing

Schmidt, D.P., et al. 2014. “Detection of cavitation in diesel fuel injector nozzles.” Engine Research Center. University of Wisconsin. Madison, Wisconsin

Smith, D. and Walker, W. 1923. “Orifice Flow”, *Proceddings of the Institution of Mechanical Engineers,* Vol 104, Issue 1, pp. 23-26

Sou A., Hosokawa S., and Tomiyama, A. 2007. “Effects of cavitation in a nozzle on liquid jet atomization”, *International Journal of Heat and Mass Transfer*, Volume 50, Issues 17–18, pp. 3575-3582

Spikes, R.H. and Pennington, G.A. 1959. “Discharge Coefficient of Small Submerged Orifices”. Archive: Proceedings of The Institution of Mechanical Engineers 1847-1982 (vols 1-196). 173. 661-674

Taylor, J.R. 1997. An Introduction To Error Analysis, 2nd ed. Sausalito, CA: University Science Books

Transit Time Ultrasonic Flow Meters, TFXL Meter User Manual, Badger Meter, Milwaukee, WI, 2016

White, F.M. 2005. “Incompressible Turbulent Mean Flow,” Viscous Fluid Flow, 3rd ed. New York, New York: McGraw-Hill

Wu Jianhua, Ai Wanzheng, and Zhou Qi, 2010, “Head loss coefficient of orifice plate energy dissipator”. *Journal of Hydraulic Research*, 48:4:526-530

Terence C. Casey V

Baltimore, MD 21217
tccasey5@gmail.com ● Cell: (302)-562-1887

EDUCATION

Johns Hopkins University **(expected) December 2017**
Baltimore, MD
M.S.E. Mechanical Engineering
Emphasis: Fluid Mechanics
Thesis: *The Design, Experimentation, and Characterization of a High-Pressure Round-Edged Orifice Plate Test Facility*

B.S. Mechanical Engineering **May 2014**
Entrepreneurship and Management Minor GPA: **3.62**

- **Dean's List**

EXPERIENCE

Johns Hopkins Applied Physics Laboratory **Laurel, MD**
Associate Engineer August 2014-Present

- Design and experimentation of subscale tests to investigate different fluid dynamics phenomenology
- Modeling and Analysis of fluids based subsystem, including heat transfer and incompressible fluid mechanics

Johns Hopkins University Mech. Eng. Dept. **Baltimore, MD**
Senior Design Department Staff June 2014-August 2014

- Completed existing design projects, including a helmet impact testing rig and an overhead crane removal system, and prepared them for delivery to their prospective clients
- Redesigned and modified existing subsystems, both mechanical and electrical, on preexisting design projects

Senior Engineering Design Project August 2013-May 2014

- Designed and built an underwater test rig for the validation of computational fluid dynamic modeling software, specifically for multiphase flow
- Researched and integrated non-visual motion tracking systems into test rig for data collection
- Developed reports and presentations for bi-monthly meetings for client feed back

Teaching Assistant August 2013-May 2014

Course: Computer-Aided Design, Heat Transfer

- Held weekly office hours to review assignments and course material
- Responsible for developing and grading assignments including exams

Johns Hopkins Applied Physics Laboratory **Laurel, MD**

Civilian Space Department Engineering Intern July 2011-July 2012

- Controlled flight simulations and supported prelaunch testing within the mission operations team of NASA's Radiation Belt Storm Probes project
- Developed operational telemetry displays and computer scripts specifically used for NASA's real-time spacecraft operations
- Monitored various subsystems and ensured health and safety requirements of the spacecraft

Awards and Honors

Departmental and General Honors 2014

Johns Hopkins University

National Mechanical Engineering Honor Society (Pi Tau Sigma) Member 2013

Naval Academy Science and Engineering Conference Scholar 2011